JGR Solid Earth

RESEARCH ARTICLE
10.1029/2019JB018878

Toward Distributed Fiber-Optic Sensing of Subsurface Deformation: A Theoretical Quantification of Ground-Borehole-Cable Interaction

Cheng-Cheng Zhang[1,2], Bin Shi[1], Hong-Hu Zhu[1], Bao-Jun Wang[1], and Guang-Qing Wei[3]

[1]School of Earth Sciences and Engineering, Nanjing University, Nanjing, China, [2]Department of Civil and Environmental Engineering, University of California, Berkeley, CA, USA, [3]Suzhou NanZee Sensing Technology Ltd., Suzhou, China

Key Points:

- A new definition of ground-cable coupling allows determining actual levels of ground deformation from fiber-optic (FO) strain measurements
- Extensive parametric analyses reveal effects of ground, borehole, backfill, and cable properties on ground-to-cable strain transfer quality
- We develop design charts and tables at designated transfer thresholds to facilitate FO instrumentation development and field deployment

Supporting Information:

- Supporting Information S1

Correspondence to:
C.-C. Zhang and B. Shi,
zhang@nju.edu.cn;
shibin@nju.edu.cn

Citation:
Zhang, C.-C., Shi, B., Zhu, H.-H., Wang, B.-J., & Wei, G.-Q. (2020). Toward distributed fiber-optic sensing of subsurface deformation: A theoretical quantification of ground-borehole-cable Interaction. *Journal of Geophysical Research: Solid Earth*, *125*, e2019JB018878. https://doi.org/10.1029/2019JB018878

Received 11 OCT 2019
Accepted 6 MAR 2020
Accepted article online 9 MAR 2020

Abstract Fiber-optic sensing is emerging as a superior means for distributed strain sensing of the subsurface. The ability of an embedded fiber-optic cable to capture accurate strain profiles depends on the degree of rigid mechanical coupling between the ground and the cable. However, a current challenge in this field is to determine the actual level of ground deformation from strain signatures sensed by the cable deployed in the subsurface; addressing this issue has been hampered by the lack of suitable theoretical methods. Here we propose a two-step ground-cable coupling evaluation procedure, whereby we develop analytical formulations to quantify the interaction and interface shear transfer of a ground-borehole-cable system. We constrain key model parameters using a data set acquired with a fiber optics-instrumented borehole for monitoring groundwater-related sediment compaction. Extensive parametric analyses reveal that increasing the backfill modulus and cable gauge length or decreasing the borehole radius and cable stiffness can improve the quality of strain transferred to the cable from the ground; the effect of ground properties is comparably insignificant. Further, we develop design charts and tables at designated transfer thresholds to facilitate the development and field deployment of fiber sensing elements. Taken together, the theoretical quantification of ground-cable coupling should improve the state-of-the-art performance of distributed fiber-optic strain sensing for subsurface ground movements detection and monitoring.

1. Introduction

Ground deformation—movements of the ground surface and subsurface strata—is a common phenomenon in nature, which accompanies a host of geological processes and human activities, such as earthquakes (Satyabala, 2006), volcanic eruptions (Brenguier et al., 2008), mass wasting (Fan et al., 2019), and subsurface resource exploitation (Barbour et al., 2016; Erban et al., 2013). Geodetic techniques used for deformation measurement include precision leveling, global navigation satellite system (GNSS), light detection and ranging (LiDAR), and interferometric synthetic aperture radar (InSAR) (Galloway & Burbey, 2011; Massonnet & Feigl, 1998). To obtain subsurface movements, field instrumentation represented by strainmeters, tiltmeters, and extensometers is commonly utilized (Amoruso et al., 2015; Peltier et al., 2006; Sleeman et al., 2000). These instruments can provide strains/displacements of subsurface formations but are currently limited by discretely instrumented measuring points, if more spatial detail is needed (Zhang et al., 2018).

Distributed fiber-optic (FO) sensing (DFOS) offers an elegant solution to this spatial undersampling problem because this technology allows measuring a near spatially continuous profile of the measurands (e.g., strain) along the entire length of an FO cable at kilometer scales and beyond (Hartog, 2017). DFOS technologies used specifically for static strain measurement are also known as distributed FO strain sensing (DFOSS), or simply distributed strain sensing (DSS). Over the past decade, DSS has asserted itself as a versatile method by which to recover the deformation of Earth materials (Buchoud et al., 2016; Habel & Krebber, 2011; Schenato, 2017; Shi et al., 2019; Zhang & Xue, 2019). Among the most widely studied are sediment compaction sensing (Murai et al., 2013; Rabaiotti et al., 2015; Zhang et al., 2018) and landslide instability detection (Denchik et al., 2019; Huntley et al., 2019; Iten et al., 2008; Kogure & Okuda, 2018; Moore et al., 2010; Picarelli et al., 2015; Puzrin et al., 2020; Schenato et al., 2017; Wang et al., 2009). For field applications, the sensing elements—FO cables—are very often installed in the ground via a trench (Hauswirth et al., 2012; Lindsey et al., 2017; Linker & Klar, 2017) or a borehole (Lellouch et al., 2019; Murai et al., 2013; Puzrin

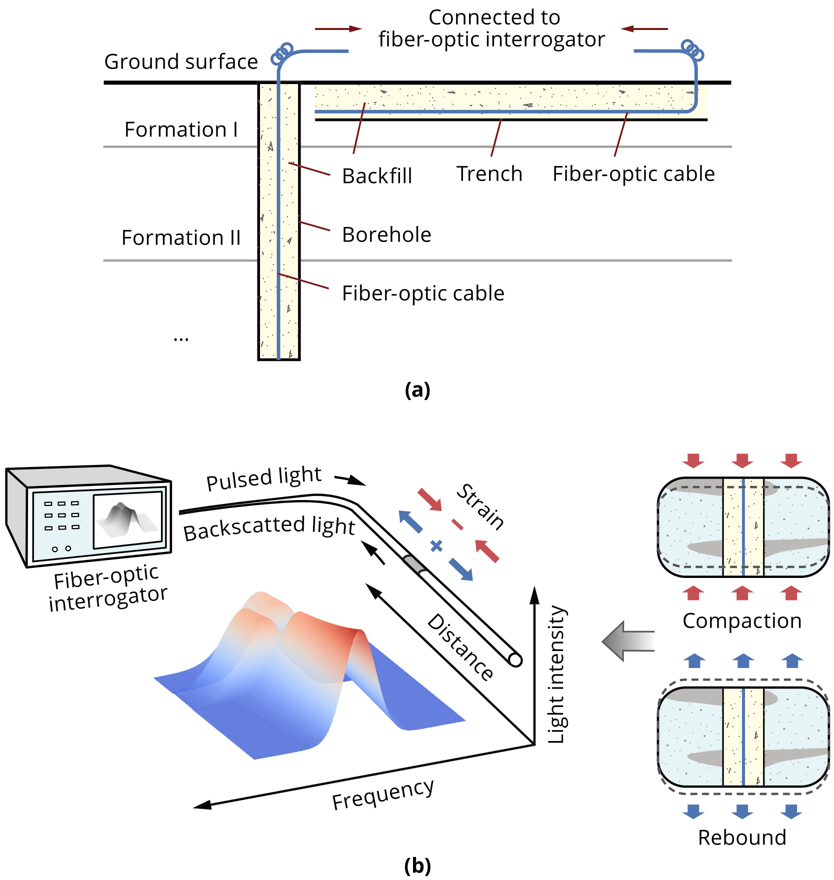

Figure 1. (a) Schematic of distributed strain sensing of the subsurface using fiber-optic cables buried in the ground. (b) Basic principle of distributed strain sensing illustrated with the example of Brillouin optical time domain reflectometry (BOTDR). "+" indicates tensile strain, and "−" indicates compressive strain, corresponding, respectively, to the rebound and compaction of a formation. Note that in addition to BOTDR, Brillouin optical time domain analysis (BOTDA), Brillouin optical frequency domain analysis (BOFDA), and Rayleigh scattering-based optical frequency domain reflectometry (OFDR) and tunable-wavelength coherent optical time domain reflectometry (TW-COTDR) have also been employed for distributed strain sensing applications.

et al., 2020; Rabaiotti et al., 2015; Zhang et al., 2018), with an optoelectronic instrument (known as the interrogator) being placed on the ground for data acquisition, as sketched in Figure 1a. The strain field transferred from the ground, through the intermediary trench or borehole, to the embedded cable results in changes in the characteristics of the light wave within the cable. Hence, demodulation of this optical signal will recover the amount of ground deformation.

Ideally, the strain sensed by the cable should be equal to the actual strain induced in the ground. In fact, the assumption that the monitored FO strain sufficiently approximates the ground strain is implicit in many practical case studies. However, the strain extracted from the demodulated signal is not fully representative of that experienced by the ground, due primarily to the interface slippage and/or the interface shear transfer within the ground-to-cable system (Zhang et al., 2018). Previous research has examined the ground-cable interface shear behavior under the pullout scenario, with particular emphasis on the progressive failure of the interface (Iten et al., 2009; Zhang et al., 2016). The deformation of an FO cable is compatible with the surrounding media provided no relative slippage occurs (governed by the shear strength criterion), as suggested by a current international standard (ASTM F3079-14, 2014). However, even though this condition is satisfied, questions remain as to whether the acquired FO strain can be related to the actual strain present in the ground. A survey of technical literature indicates that the strain transfer issue has been investigated previously in the field of structural health monitoring based primarily on the shear lag theory (Ansari &

Yuan, 1998; LeBlanc, 1999; Li et al., 2009), but the interaction mechanism and mechanical coupling of an embedded FO cable with surrounding geological formations are not clearly understood.

This study aims to provide a theoretical approach for interpretation of the actual level of ground deformation from the strain data measured by an FO cable directly buried in the ground and to offer practical suggestions on the choice of cable and borehole backfill. The article focuses on DSS and is organized as follows. Section 2 provides background information on the DSS measurement principle. The ground-cable coupling evaluation procedure and analytical formulations are detailed in section 3. Extensive parametric analyses of ground-cable interface bond and strain transfer are given in section 4. In section 5, design charts and tables are developed and recommendations are provided for cable development and backfill selection. Section 6 presents a concise discussion of the results. Finally, section 7 summaries findings drawn from this work.

2. Principle of DSS for Deformation Measurement

DFOS allows measuring the spatial profile of one or more measurands (e.g., strain, temperature, vibration) at each and every point along an FO cable. Because the cable is itself both the transmission medium and the sensing element, no extra transducers are needed along the optical path. By exploiting the naturally occurring Brillouin or Rayleigh backscattering phenomenon, static and dynamic strain sensing can be achieved. Here, the strain refers to the axial strain if not otherwise stated. Brillouin scattering-based technologies such as Brillouin optical time domain reflectometry/analysis (BOTDR/A) are commonly employed for DSS purposes (Soga & Luo, 2018). Also being increasingly used are Rayleigh-based optical frequency domain reflectometry (OFDR) and tunable-wavelength coherent optical time domain reflectometry (TW-COTDR), featured with very high spatial resolution (SR) (Kogure & Okuda, 2018; Kwon et al., 2018; Lanticq et al., 2009; Schenato et al., 2017; Zhang & Xue, 2019). The sensing principle described below is based on the popular BOTDR technology (Bao & Chen, 2012; Horiguchi et al., 1989; Thévenaz, 2010).

When a pulse of light generated by an FO interrogator travels through the cable, Brillouin scattering occurs at any point along the cable. The signal resulting from Brillouin scattering, with a shift of its frequency, propagates back toward the optical source, as shown in Figure 1b. A linear relationship exists between the frequency shift of the Brillouin backscatter and the strain or temperature, which is given by

$$\Delta\nu_{\mathrm{B}} = C_{\mathrm{e}}\Delta\varepsilon + C_{\mathrm{T}}\Delta T \tag{1}$$

where $\Delta\nu_{\mathrm{B}}$ is the measured change in Brillouin frequency shift; $\Delta\varepsilon$ and ΔT are the changes in strain and temperature, respectively; C_{e} is the calibrated Brillouin frequency shift-strain coefficient of an FO strain sensing cable; and C_{T} is the calibrated Brillouin frequency shift-temperature coefficient. Because the Brillouin frequency shift is sensitive to both strain and temperature variations, temperature compensation for the measured data needs to be performed. This can be accomplished by deploying an extra temperature sensing cable (insensitive to mechanical strains) adjacent to the strain sensing cable. Assume the colocated temperature sensing cable has a temperature coefficient of $C_{\mathrm{T}}^{\mathrm{T}}$, the Brillouin frequency shift due to thermal fluctuations is $\Delta\nu_{\mathrm{B}}^{\mathrm{T}} = C_{\mathrm{T}}^{\mathrm{T}}\Delta T$. By eliminating this thermal effect, the real strain caused by ground deformation is given by

$$\Delta\varepsilon = \frac{1}{C_{\mathrm{e}}}\left(\Delta\nu_{\mathrm{B}} - C_{\mathrm{T}}\Delta T\right) = \frac{1}{C_{\mathrm{e}}}\left(\Delta\nu_{\mathrm{B}} - \frac{C_{\mathrm{T}}}{C_{\mathrm{T}}^{\mathrm{T}}}\Delta\nu_{\mathrm{B}}^{\mathrm{T}}\right) \tag{2}$$

Since the cable can sense both tensile and compressive strains, by using equation 2 a continuous profile of ground deformation (rebound or compaction, or both) can be mapped. Further details of the DSS technology for deformation measurement may be found in Schenato et al. (2017).

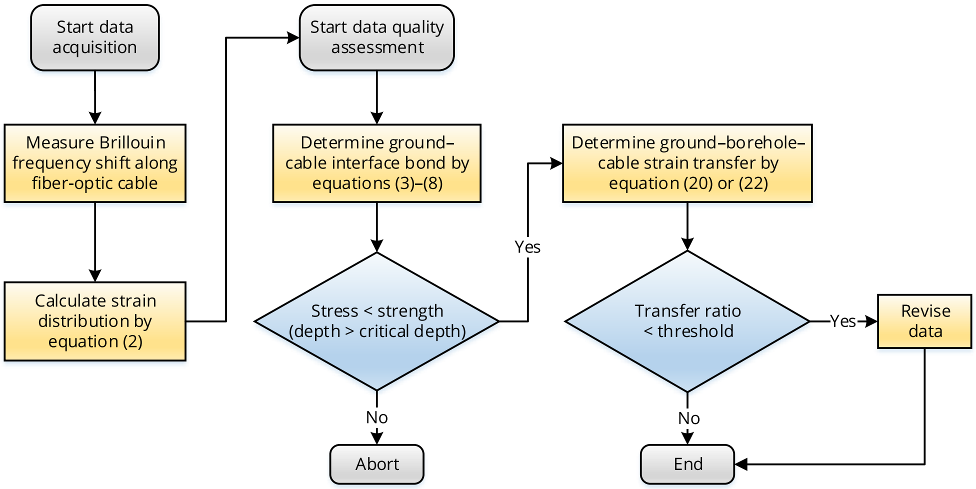

Figure 2. A flowchart for the retrieval of true ground deformation from distributed strain signatures, illustrated with Brillouin scattering-based technologies. Brillouin frequency shifts measured from strain sensing cables should be temperature compensated, for example, via a colocated temperature sensing cable before converting to a strain profile. The cable interior (cable-to-fiber) strain transfer efficiency can be quantified and calibrated, and incorporated into the frequency shift-strain coefficient (an interrogator input parameter). Hence, the focus here is on the ground-to-cable strain transfer loss; the cable includes jacket, reinforcement, buffer, cladding, and fiber core as a single system.

3. Methodology

For structural health monitoring FO strain sensing cables are either bonded to the surface of man-made structures or directly embedded during the production of test elements by using adhesives. By contrast, ground deformation monitoring using DSS is characterized by the following features:

- FO cables are installed in trenches or boreholes (Figure 1a) in which the backfills are the excavated soils, non–in situ Earth materials, or bentonite cement grout. Due to lack of standardized procedures for cable installation and backfilling, it is unclear whether ground movement-induced strains are wholly transferred to the cable.
- The ground is heterogeneous and anisotropic; the physical properties (e.g., density and water content) of the shallow subsurface are readily influenced by the environment. Especially, the confining pressure can vary from zero to several megapascals from the ground surface to a depth of a few hundred meters. Thus, there may be interface slippage between the cable and surrounding Earth materials under low densities, high water contents, or low confining pressures.

To limit the extent of the study, we here focus on borehole deployments. Given all the characteristics described above, a good coupling between the ground and fiber should fulfill two requirements: (1) perfect bonds exist at all interfaces including the ground-borehole and borehole-cable interfaces, and (2) strains induced in the ground can transfer efficiently to the fiber core. Thus, the assessment of temperature-compensated strain data should also follow two steps (Figure 2). The interface bond is determined first, and then, if the interface shear strengths have not yet been reached, a strain transfer ratio is calculated to correct the acquired FO strains. These two issues are dealt with in sections 3.1 and 3.2, respectively.

3.1. Ground-Borehole-Cable Interface Bond

FO strain sensing cables for field applications are often well protected to survive in harsh geologic and construction environments; the resultant cable Young's modulus is typically within the range 0.3–75 GPa (Iten et al., 2011). Due to the modulus difference among the cable, backfilled materials, and ground, slippage is likely to occur at the corresponding interfaces. In this section, the focus is on the borehole (backfill)-cable interface bond.

Laboratory pullout tests showed that a backfill-cable interface may exhibit strain-softening or strain-hardening behavior depending on backfill properties (Zhang et al., 2016). Although the backfill-cable interface remains partially bonded after the peak interface shear strength is reached, the reliability of monitored FO data cannot be guaranteed and so the critical-state interface shear strength is not considered. Experimental evidence indicated that the classical Mohr-Coulomb failure criterion holds for the backfill-cable interface, which is given by (Zhang et al., 2016)

$$\tau_c^p = c_c + \sigma_c \tan\delta_c \tag{3}$$

where τ_c^p, c_c, and δ_c are the peak interface shear strength, cohesion, and friction angle of the backfill-cable interface, respectively, and σ_c is the confining pressure applied to the backfill-cable interface. For the vertically buried cable, σ_c can be calculated by

$$\sigma_c = K\gamma_g h \tag{4}$$

where γ_g is the bulk unit weight of the overlying ground; h is the depth below the ground surface; and K is the coefficient of lateral Earth pressure.

The backfill-cable interface shear stress can be estimated using (Zhang et al., 2016)

$$\tau_c = \frac{E_c A_c}{2\pi r_c} \frac{d\varepsilon}{dz} \tag{5}$$

where E_c, A_c, and r_c are the Young's modulus, cross-sectional area, and radius of the FO cable, respectively; ε is the monitored strain; and $d\varepsilon/dz$ is the gradient of the monitored strain, which can be estimated by

$$\frac{d\varepsilon}{dz} \approx \frac{\Delta\varepsilon}{\Delta z} \tag{6}$$

where $\Delta\varepsilon$ is the difference in strain between two adjacent measuring points and Δz is the spatial sampling interval.

Normally, no backfill-cable slippage would occur provided that the following inequality holds: $\tau_c < \tau_c^p$ (ASTM F3079-14, 2014). To go further, a critical confining pressure, $\sigma_{c,cr}$, or depth, h_{cr}, may be proposed. Substitution of equation 5 into equation 3 yields

$$\sigma_{c,cr} = \frac{E_c A_c}{2\pi r_c \tan\delta_c} \left[\frac{d\varepsilon}{dz}\right]_m - \frac{c_c}{\tan\delta_c} \tag{7}$$

$$h_{cr} = \frac{E_c A_c}{2\pi r_c K \gamma_g \tan\delta_c} \left[\frac{d\varepsilon}{dz}\right]_m - \frac{c_c}{K\gamma_g \tan\delta_c} \tag{8}$$

where $[d\varepsilon/dz]_m$ is the maximum strain gradient. As $[d\varepsilon/dz]_m$ decreases, a smaller $\sigma_{c,cr}$ or h_{cr} is required to guarantee a perfect backfill-cable interface bond which is desirable in practice.

3.2. Ground-Borehole-Cable Strain Transfer

Once the interface shear stress state is determined the strain transfer from the ground to the cable should be further considered. Because the FO cable is itself a multilayered composite, the total strain transfer ratio, η, may be considered to comprise two ratios:

$$\eta = \alpha \cdot \beta \tag{9}$$

where α quantifies the strain transfer among the ground, backfill, and FO cable and is the focus of this investigation, whereas β characterizes the strain transfer within the FO cable, which is commonly calibrated by the cable manufacturer and can be incorporated into the aforementioned frequency shift-strain coefficient.

The following derivation is based on classical strain transfer models (e.g., Ansari & Yuan, 1998; LeBlanc, 1999; Li et al., 2009; Xiang & Wang, 2018) originally developed within the context of structural health monitoring. To address the current physical problem (ground-borehole-cable interaction),

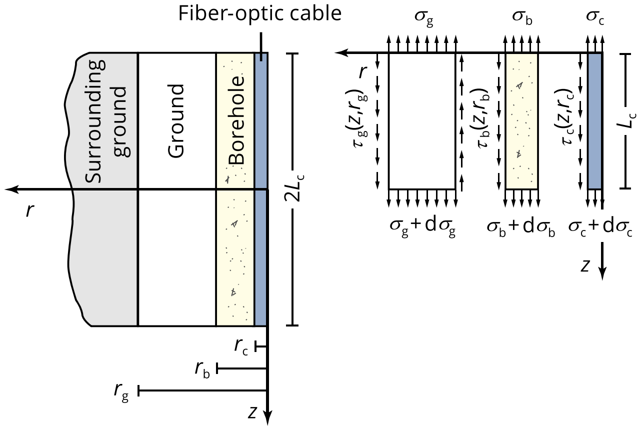

Figure 3. Interaction and interface shear transfer among ground, borehole, and a fiber-optic strain sensing cable deployed in a vertical borehole (dimensions not to scale). r, τ, and σ represent radius, shear stress, and normal stress, respectively. Subscripts, g, b, and c, denote ground, borehole backfill, and cable, respectively. $2L_c$ = cable gauge length; z = distance from cable center.

modification of the model formulation has been made pertinent to the cable type and borehole-cable interface property. Figure 3 shows a segment of FO cable with a length of $2L_c$ embedded in the borehole in a direction parallel to the ground movement, together with a reference frame describing the coordinates, dimensions, and normal and shear stresses. In this figure and the following derivations, r, w, and u represent the radius, radial displacement, and axial displacement, respectively; τ, σ, and ε represent the shear stress, normal stress, and normal strain, respectively; G, E, and μ represent the shear modulus, Young's modulus, and Poisson's ratio, respectively; and the subscripts, g, b, and c, denote the ground, borehole backfill, and cable, respectively. Additionally, the basic simplifying assumptions pertaining to the model formulation are that each layer behaves linearly elastically and all the interfaces bond perfectly. These indicate equivalent shear stresses or displacements at the interfaces (the boundary conditions).

Summing the forces acting on an element of the FO cable, the following relationship is found between the normal stress and shear stress:

$$\frac{\partial \sigma_c(z)}{\partial z} = -\frac{2\tau_c(z, r_c)}{r_c} \tag{10}$$

Analogously, force equilibrium of the backfill ($r_c \le r \le r_b$) and ground ($r_b \le r \le r_g$) yields

$$\tau_b(z, r) = -\frac{\partial \sigma_c(z)}{\partial z}\frac{r_c^2}{2r} - \frac{\partial \sigma_b(z)}{\partial z}\frac{r^2 - r_c^2}{2r} \tag{11}$$

$$\tau_g(z, r) = -\frac{r_c^2}{2r}\frac{\partial \sigma_c(z)}{\partial z} - \frac{\partial \sigma_b(z)}{\partial z}\frac{r_b^2 - r_c^2}{2r} - \frac{\partial \sigma_g(z)}{\partial z}\frac{r^2 - r_b^2}{2r} \tag{12}$$

The shear stresses are alternatively written in terms of the shear modulus and displacements:

$$\tau_b(z, r) = G_b\left(\frac{\partial u_b(z, r)}{\partial r} + \frac{\partial w_b(z, r)}{\partial z}\right) \tag{13}$$

$$\tau_g(z, r) = G_g\left(\frac{\partial u_g(z, r)}{\partial r} + \frac{\partial w_g(z, r)}{\partial z}\right) \tag{14}$$

Assuming negligible radial deformation ($\partial w/\partial z = 0$), the normal stresses in equations 11 and 12 are correlated to the u displacements in equations 13 and 14. The resulting two expressions are integrated, over r, from r_c to r_b and r_b to r_g, respectively, which yields

$$\Delta u_\mathrm{c} = -\frac{1}{G_\mathrm{b}}\left[\left(\frac{r_\mathrm{b}^2 - r_\mathrm{c}^2}{4} - \frac{r_\mathrm{c}^2}{2}\ln\frac{r_\mathrm{b}}{r_\mathrm{c}}\right)\frac{\partial\sigma_\mathrm{b}(z)}{\partial z} + \frac{r_\mathrm{c}^2}{2}\ln\frac{r_\mathrm{b}}{r_\mathrm{c}}\frac{\partial\sigma_\mathrm{c}(z)}{\partial z}\right] \tag{15}$$

$$\Delta u_\mathrm{b} = -\frac{1}{G_\mathrm{g}}\left[\left(\frac{r_\mathrm{g}^2 - r_\mathrm{b}^2}{4} - \frac{r_\mathrm{b}^2}{2}\ln\frac{r_\mathrm{g}}{r_\mathrm{b}}\right)\frac{\partial\sigma_\mathrm{g}(z)}{\partial z} + \ln\frac{r_\mathrm{g}}{r_\mathrm{b}}\left(\frac{r_\mathrm{b}^2 - r_\mathrm{c}^2}{2}\frac{\partial\sigma_\mathrm{b}(z)}{\partial z} + \frac{r_\mathrm{c}^2}{2}\frac{\partial\sigma_\mathrm{c}(z)}{\partial z}\right)\right] \tag{16}$$

where Δu_c is the relative displacement between the backfill and cable and Δu_b between the ground and backfill.

Classical strain transfer models for a structure-protective layer-fiber core system are commonly based on the shear lag theory under the assumptions that the Young's modulus of the middle layer is orders of magnitude lower than that of the fiber core and that their radiuses are comparable (e.g., Ansari & Yuan, 1998; Li et al., 2009). This, however, is not the case in our problem as the radius of the "middle layer" (i.e., the borehole backfill) can be up to 65 times that of the FO cable (Zhang et al., 2018). Alternatively, Goodman's hypothesis—a linear constitutive relation between interface shear stress and relative displacement—has been successfully introduced to quantify the interfacial contacting state of an asphalt pavement-protective layer-fiber core system (Xiang & Wang, 2018). This assumption is employed in this study under which two different formulations are obtained.

If the borehole-cable interface property is considered, the governing equation for the ground-borehole-cable strain transfer is derived as (see section A1)

$$\frac{1}{\lambda_1^2}\varepsilon_\mathrm{c}'' - \varepsilon_\mathrm{c} = -\varepsilon_\mathrm{g} \tag{17}$$

where λ_1 is a parameter encapsulating the effects of geometry and modulus of the cable and backfill and the adhesion coefficients of the interfaces, having the following form:

$$\lambda_1 = \left[\frac{E_\mathrm{c} r_\mathrm{c}}{2k_\mathrm{c}} + \frac{E_\mathrm{c} r_\mathrm{c}^2}{2k_\mathrm{b} r_\mathrm{b}} + \frac{E_\mathrm{c}\left(r_\mathrm{b}^2 - r_\mathrm{c}^2\right)\left(E_\mathrm{b} r_\mathrm{c} - 2(1+\mu_\mathrm{b})k_\mathrm{c} r_\mathrm{c}^2 \ln\frac{r_\mathrm{b}}{r_\mathrm{c}}\right)}{2k_\mathrm{b} k_\mathrm{c} r_\mathrm{b}(1+\mu_\mathrm{b})\left(r_\mathrm{b}^2 - r_\mathrm{c}^2 - 2r_\mathrm{c}^2 \ln\frac{r_\mathrm{b}}{r_\mathrm{c}}\right)}\right]^{-\frac{1}{2}} \tag{18}$$

Here we consider a fixed-point or microanchored design for the FO cable which transforms the cable into multiple sensors in series; the distance between two neighboring fixation points or microanchors is referred to as gauge length, $2L_\mathrm{c}$ (supporting information Figure S1). The ground-borehole-cable strain transfer ratio, α, and its averaged value, $\overline{\alpha}$, over the gauge length is readily obtained as

$$\alpha = 1 - \frac{\cosh(\lambda_1 z)}{\cosh(\lambda_1 L_\mathrm{c})} \tag{19}$$

$$\overline{\alpha} = 1 - \frac{\tanh(\lambda_1 L_\mathrm{c})}{\lambda_1 L_\mathrm{c}} \tag{20}$$

If the effect of ground property is taken into consideration, α and $\overline{\alpha}$ are respectively derived as (see section A2)

$$\alpha = \kappa_2\left(1 - \frac{\cosh(\lambda_2 z)}{\cosh(\lambda_2 L_\mathrm{c})}\right) \tag{21}$$

$$\overline{\alpha} = \kappa_2\left(1 - \frac{\tanh(\lambda_2 L_\mathrm{c})}{\lambda_2 L_\mathrm{c}}\right) \tag{22}$$

where λ_2 and κ_2 have the following forms:

$$\lambda_2 = \left[\frac{E_\mathrm{c}}{E_\mathrm{b}} r_\mathrm{c}^2 (1+\mu_\mathrm{b})\left(\frac{r_\mathrm{b}^2}{r_\mathrm{b}^2 - r_\mathrm{c}^2}\ln\frac{r_\mathrm{b}}{r_\mathrm{c}} - \frac{1}{2}\right)\right]^{-\frac{1}{2}} \tag{23}$$

$$\kappa_2 = 1 - \frac{(\chi-1)k_\mathrm{g}r_\mathrm{g}\left(\ln\frac{r_\mathrm{g}}{r_\mathrm{b}} - \frac{E_\mathrm{g}}{2k_\mathrm{b}r_\mathrm{b}\left(1+\mu_\mathrm{g}\right)}\right)}{\frac{r_\mathrm{g}^2 - r_\mathrm{b}^2}{4} - \frac{r_\mathrm{g}^2}{2}\ln\frac{r_\mathrm{g}}{r_\mathrm{b}} + \frac{\left(1+\mu_\mathrm{g}\right)\left(r_\mathrm{g}^2 - r_\mathrm{b}^2\right)}{k_\mathrm{b}r_\mathrm{b}E_\mathrm{g}}} \cdot$$

$$\left[\frac{(1+\mu_\mathrm{b})\left(r_\mathrm{g}^2 - r_\mathrm{b}^2\right)}{E_\mathrm{b}}\left(\frac{1}{4} - \frac{r_\mathrm{c}^2}{2\left(r_\mathrm{b}^2 - r_\mathrm{c}^2\right)}\ln\frac{r_\mathrm{b}}{r_\mathrm{c}}\right) + \frac{1+\mu_\mathrm{g}}{E_\mathrm{g}}\left(r_\mathrm{g}^2\ln\frac{r_\mathrm{g}}{r_\mathrm{b}} - \frac{r_\mathrm{g}^2 - r_\mathrm{b}^2}{2}\right)\right] \tag{24}$$

$$-2(\chi-1)k_\mathrm{g}r_\mathrm{g}\left[\frac{1+\mu_\mathrm{g}}{E_\mathrm{g}}\ln\frac{r_\mathrm{g}}{r_\mathrm{b}} + \frac{1+\mu_\mathrm{b}}{E_\mathrm{b}}\left(\frac{1}{2} - \frac{r_\mathrm{c}^2}{r_\mathrm{b}^2 - r_\mathrm{c}^2}\ln\frac{r_\mathrm{b}}{r_\mathrm{c}}\right)\right]$$

In summary, two separate expressions for the ground-borehole-cable strain transfer ratio are obtained using different equilibrium conditions. The former allows the consideration of the influence of borehole-cable interface adhesion, whereas the latter can be used for quantifying the effects of ground properties including the ground modulus and ground-borehole interface adhesion. Note that when $\chi = 1$, namely the surrounding ground and the ground under investigation is considered as a whole, κ_2 vanishes and only the geometry and stiffness of the cable and borehole backfill need to be determined. Hence, the latter expression is especially favorable in practice, serving as a first approximation of the ground-to-cable strain transfer ratio provided the ground and interface properties are not readily available.

3.3. Validation and Performance Evaluation

Before carrying out a parametric analysis, the validity of theoretical developments leading to the analytical expressions of ground-borehole-cable strain transfer ratio needs to be verified. This is accomplished by comparison to existing theoretical models (Ansari & Yuan, 1998; LeBlanc, 1999; Li et al., 2009) that are adapted for addressing the current physical problem. The parameters used for the comparison are summarized in Table S1, but the selection of their values is discussed in the subsequent section 4.1. Results from the comparison are presented as a matrix of four plots in Figure S2. The left plots represent the distribution of strain transfer ratio, α, along the FO cable, whereas the right plots depict the variation of average strain transfer ratio, $\overline{\alpha}$, as a function of the gauge length, $2L_\mathrm{c}$. The top and bottom rows correspond to strong and weak adhesions at interfaces, respectively, which are represented by high or low interface adhesion coefficients.

For the case of strong adhesions at the ground-borehole and borehole-cable interfaces, good agreement between this work and the three analytical solutions from the literature is observed (Figures S2a and S2b). However, there is some loss of consistency observed at short gauge lengths for Ansari and Yuan's solution. This likely is due to the simplifying assumption made in their analysis—the strain is perfectly transferred at the midlength of the cable, that is, $\alpha|_{z=0} = 1$, which leads to an overestimation of strain transfer when the gauge length is relatively short. As the interface adhesion gets weaker, it is obvious both conceptually and from our calculations presented in Figures S2c and S2d that the quality of transfer decreases. By contrast, the transfer ratios calculated by classical models remain unchanged irrespective of interface adhesion variation. This is expected as the effect of interface properties was not considered in these models, indicating that they may not be applicable to cases of low interface adhesions. However, as the gauge length increases the difference in calculations becomes less and the data converges to an average ratio of unity (Figure S2d).

4. Parametric Analysis

A parametric sensitivity analysis of ground-cable interface bond and strain transfer is undertaken in this section. To keep the scope of the investigation manageable, the analysis is limited to consideration of the following 15 parameters: ground property parameters (γ_g, E_g, μ_g, and K), borehole and backfill property parameters (r_b, E_b, and μ_b), ground-borehole interface adhesion coefficient (k_b), cable property parameters (L_c, r_c, and E_c), borehole-cable interface parameters (δ_c, c_c, and k_c), and maximum strain gradient ($[\mathrm{d}\varepsilon/\mathrm{d}z]_\mathrm{m}$). While

Table 1
Three Fiber-Optic Strain Sensing Cables Designed for Ground Deformation Measurement

Cable	DSS-C1	DSS-C2	DSS-C3
Type	Tight-buffered, TPU-jacketed	Tight-buffered, steel strand-reinforced, PE-jacketed	Tight-buffered, glass fiber-reinforced, PE-jacketed
Schematic cross section	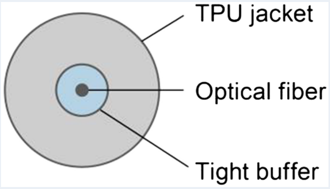	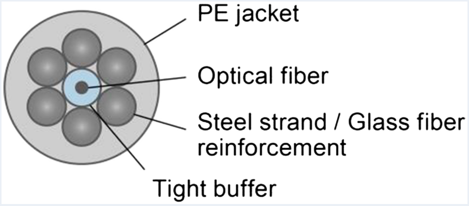	
Radius (mm)	1	2.5	2.9
Weight (kg/km)	2	38	24.5
Young's modulus (GPa)	0.37	21.67	28.00
Axial stiffness (kN)	1.2	425.5	739.8
Feature description	• Can be readily prestrained and directly integrated into loose materials such as the topsoil • Can withstand moderate impacts during installation	• Can survive in harsh environmental conditions because of high mechanical performance • Well suited for monitoring subsurface formation movements	

Note. The optical fiber depicted consists of a fiber core (silica core and cladding collectively) and a coating. Axial stiffness is equivalent to Young's modulus multiplied by cross-sectional area. For distributed strain sensing applications a fixed-point or microanchored design is considered for the cables (Figure S1). TPU = thermoplastic polyurethane; PE = polyethylene.

other factors (e.g., χ, r_g, and k_g) may also affect ground-borehole-cable coupling, these are considered likely to be of secondary importance; hence, consideration of their influences is deferred to future studies.

4.1. Selection of Parameter Values

4.1.1. Ground, Borehole, and Ground-Borehole Interface Properties

In the current investigation, typical geological formations from unconsolidated sediments to rock strata are considered and so γ_g ranging from 16 to 33 kN/m^3, E_g between 0.01 and 100 GPa, and μ_g of 0.06–0.45 are employed. Given the influence of drilling and backfilling, the radius of ground, r_g, is set to 4 times the radius of borehole, r_b (Li et al., 2009). Since the deformation gradient in the radial direction is relatively small compared to that along the cable axis, a χ of 1.1 should be reasonable. The coefficient of lateral Earth pressure, K, exerted on the vertical cable is dependent on how the cable interacts with the ground. Although installation of the cable may potentially disturb the stress state of the surrounding ground, to limit the complexity of the analysis the coefficient of Earth pressure at rest ranging from 0.3 to 1 for soils or 0.1 to 0.7 for rocks is assumed.

High-quality backfilling is essential for guaranteeing that the ground deformation would be felt by the cable. Rabaiotti et al. (2015) reported using a cement-bentonite grout of similar stiffness as surrounding soils to backfill and seal a borehole embedded with an FO vertical extensometer. A mixture of sand and clay was employed by Zhang et al. (2018) to backfill a 200 m deep, 64.5 mm radius borehole; the borehole was left to rest over a month to allow the backfill and ground to contract around the embedded FO cable. Despite lack of standardized backfilling procedure, current practice indicates that FO borehole backfilling materials are of similar stiffness as surrounding strata and so E_b and μ_b are considered to be within 0.01–40 GPa (Plinninger et al., 2010) and 0.15–0.45, respectively. The radius of borehole, r_b, is assumed to range from 25 to 200 mm (Kogure & Okuda, 2018; Zhang et al., 2018), and the ground-borehole interface adhesion coefficient, k_b, from 1 to 1,000 GPa/m (Xiang & Wang, 2018).

4.1.2. Cable and Borehole-Cable Interface Properties

As mentioned earlier, FO strain sensing cables for ground deformation monitoring often have multilayer buffer and sheath to increase their robustness. The Young's modulus, E_c, of a buffered cable may vary significantly depending on whether metal tubes, stranded stainless steel wires, or fiber-reinforced polymers are

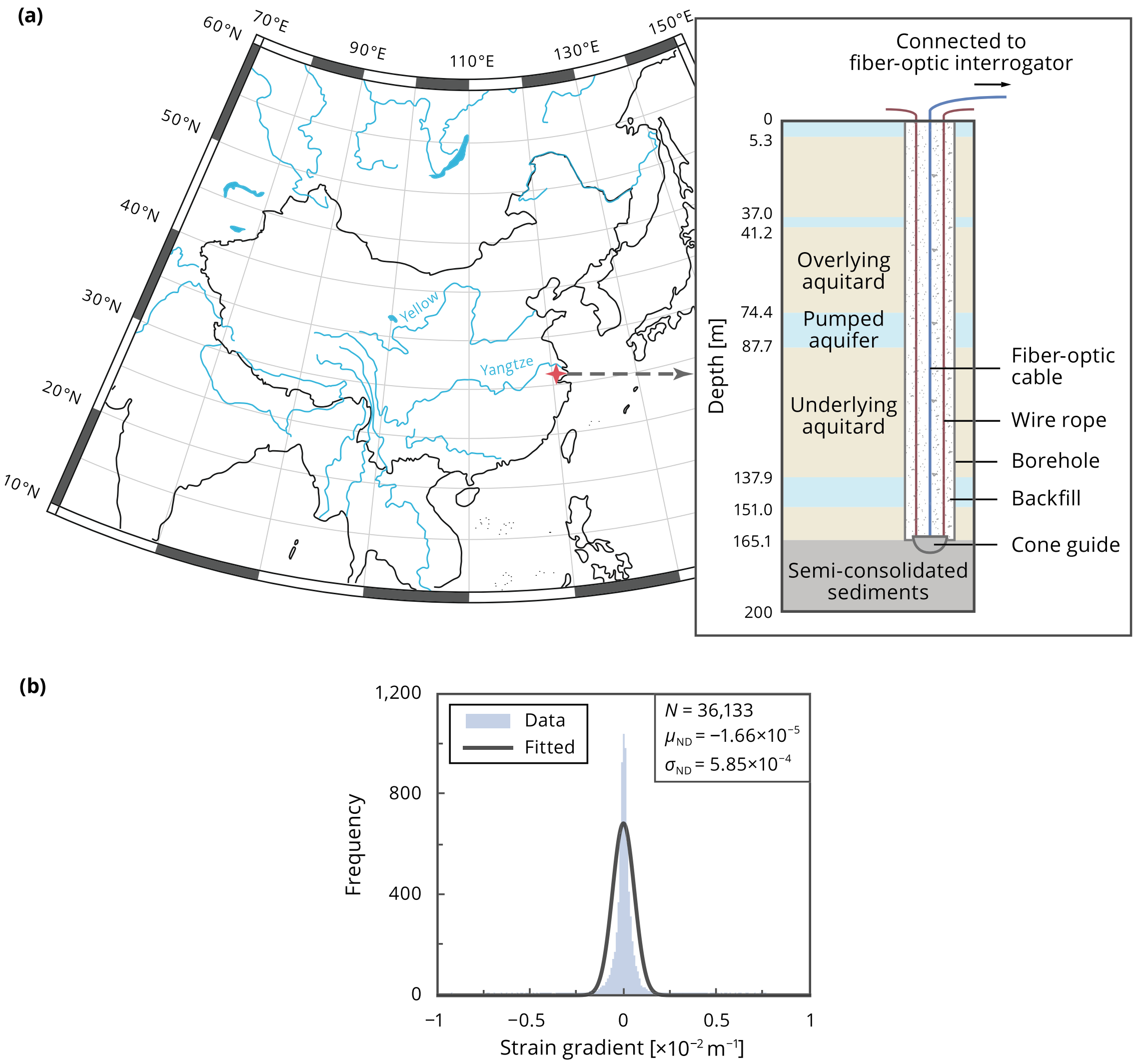

Figure 4. (a) A fiber optics-instrumented borehole for monitoring groundwater-related sediment compaction in Shengze (southern Yangtze Delta, China). Red marker indicates borehole location (30°53′23.96″N, 120°40′47.11″E). See Zhang et al. (2018) for details on field deployment of fiber-optic instrumentation. (b) Strain gradient estimated using a near 2-year data set (total data amount $N = 36{,}133$). Strains were measured using a tight-buffered, thermoplastic polyurethane (TPU)-jacketed cable (DSS-C1; Table 1) deployed in the borehole. Positive and negative strains denote tensile and compressive strains, respectively. The strain gradient does not exceed 2×10^{-3} m^{-1} according to Gaussian fitting ($\mu_{\mathrm{ND}} \pm 3\sigma_{\mathrm{ND}}$ is within the range -1.77×10^{-3} to 1.74×10^{-3} m^{-1}).

employed. Generally though, E_c between 0.3 and 75 GPa and r_c between 0.45 and 4.5 mm were commonly reported (Iten et al., 2011; Lienhart, 2015; Schenato et al., 2017). Consequently, $E_c r_c$ ranging from 0.3 to 120 MN/m is analyzed in the current investigation. For field applications, the gauge length, $2L_c$, of a cable is considered to range from 0.1 to 20 m. In particular, three specially designed tight-buffered FO cables for ground deformation sensing are investigated: a 1 mm radius tight-buffered, thermoplastic polyurethane (TPU)-jacketed cable (DSS-C1), a 2.5 mm radius steel strand-reinforced cable (DSS-C2), and a 2.9 mm radius glass fiber-reinforced cable (DSS-C3). DSS-C1 has a relatively low modulus due to the soft TPU jacket and so it can be easily prestrained and directly installed in loose materials such as a soil. DSS-C2 and DSS-C3, by contrast, are respectively reinforced by stranded stainless steel wires and fiber-reinforced polymers, allowing survival in harsh geologic environments. The physical and mechanical parameters of the three cables are listed in Table 1.

Data available in the research literature (Zhang et al., 2016), though of limited scope indicates that the tangent of the friction angle, $\tan\delta_c$, of a sand-cable interface is within the range 0.45–0.75 and the cohesion, c_c, is between 0 and 45 kPa. For backfills of higher modulus such as a cement-like material, the interface cohesion

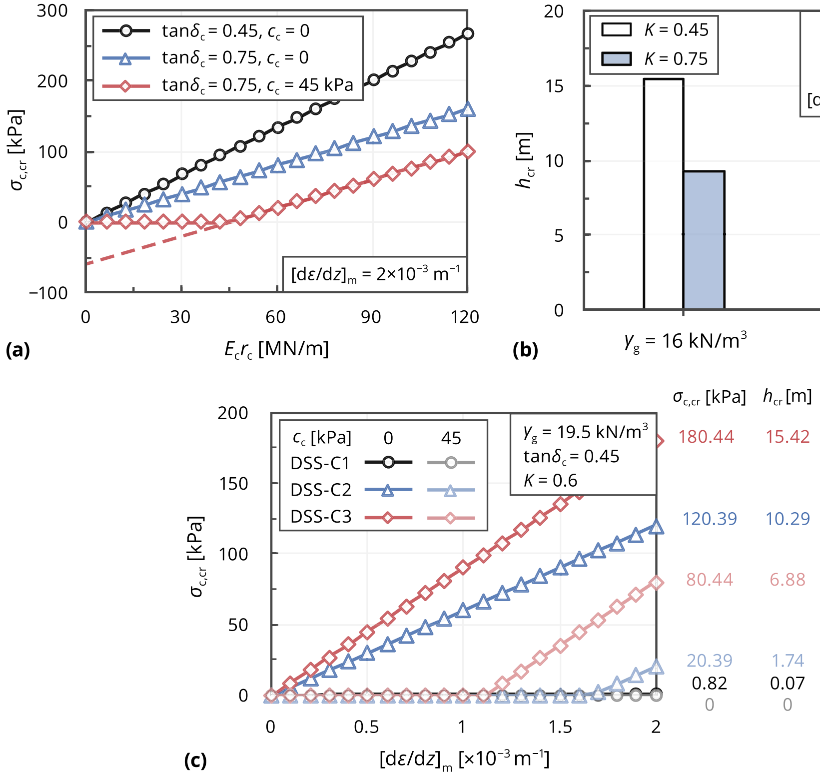

Figure 5. Sensitivity of critical confining pressure ($\sigma_{c,cr}$) or depth (h_{cr}) to the variation of ground (γ_g and K), cable (E_c and r_c), and backfill-cable interface (δ_c and c_c) parameters and maximum strain gradient ([dε/dz]$_m$), in cases of strain sensing of unconsolidated sediments. Negative $\sigma_{c,cr}$ values represented by the dashed line in (a) indicate that interface cohesion c_c alone is sufficient to ensure interface bonding for a given [dε/dz]$_m$, and so these values should be revised to 0. (b) Effects of γ_g and K on h_{cr}. In (c), $\sigma_{c,cr}$ and h_{cr} values are presented at a [dε/dz]$_m$ of 2×10^{-3} m^{-1}. With regard to rock formations, cement-like materials are commonly used for borehole backfilling and so interface decoupling is unlikely to be a major concern. Parameters other than those investigated are also shown in each plot.

should be increased accordingly. The sand-cable interface adhesion coefficient, k_c, is assumed to range from 0.05 to 5 GPa/m (Zhang et al., 2016).

4.1.3. Strain Gradient

Like the ground-borehole interface adhesion coefficient, reporting of typical ranges for the gradient of monitored FO strain is particularly scarce in the literature. However, a DSS system deployed in Shengze (southern Yangtze Delta, China) for groundwater-related settlement monitoring (Zhang et al., 2018; Figure 4a) has provided huge data sets to constrain the strain gradient. A near 2-year data set (total amount of data N = 36,133) reporting strain values measured from the aforementioned 1 mm radius tight-buffered, TPU-jacketed cable is analyzed (Figure 4b). The observed data appear to have a normal distribution and $\mu_{ND} \pm 3\sigma_{ND}$ is within the range -1.77×10^{-3} to 1.74×10^{-3} m^{-1}, indicating that the strain gradient seldom exceeds 2×10^{-3} m^{-1}.

4.2. Parametric Analysis Results—Interface Bond

The parametric analysis investigates the sensitivity of critical confining pressure ($\sigma_{c,cr}$) or depth (h_{cr}) to the variation of ground (γ_g and K), cable (E_c and r_c), and backfill-cable interface (δ_c and c_c) parameters and maximum strain gradient ([dε/dz]$_m$), in cases of strain sensing of unconsolidated sediments (Figure 5). With regard to rock formations, cement-like materials are commonly used for borehole backfilling and so interface decoupling between the cable and surrounding medium is unlikely to be a major concern. To assist compact presentation of the results, each plot consists of two or three factors investigated; parameters other than those investigated are also shown in each plot.

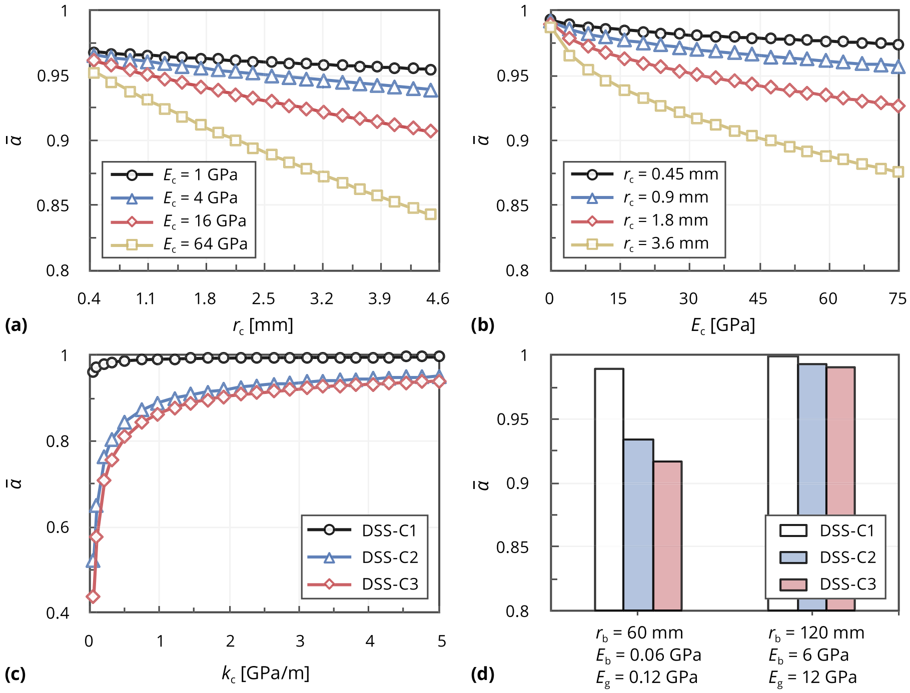

Figure 6. Effects on the average ground-borehole-cable strain transfer ratio ($\overline{\alpha}$) of variations in (a) radius of fiber-optic cable (r_c); (b) Young's modulus of fiber-optic cable (E_c); and (c) borehole-cable interface adhesion coefficient (k_c). (d) $\overline{\alpha}$ values for three fiber-optic strain sensing cables under two typical ground and borehole conditions. r_b = borehole radius; E_b = backfill Young's modulus. Parameters other than those investigated are summarized in Table 2.

From Figure 5a, it may be readily observed that lower $E_c r_c$ values or larger δ_c or c_c values correspond to a smaller $\sigma_{c,cr}$ and, hence, also a smaller h_{cr}. One may note negative $\sigma_{c,cr}$ values accompanying small $E_c r_c$ represented by a dashed line for the case of $\tan\delta_c = 0.75$ and $c_c = 45$ kPa. This is due to the interface cohesion effect and also indicates that the interface shear stress, τ_c, is always less than the strength, τ_c^p, at a $[\mathrm{d}\varepsilon/\mathrm{d}z]_\mathrm{m}$ of 2×10^{-3} m^{-1}. Obviously, these negative values should be revised to 0, which bears some resemblance to active Earth pressure calculation using the classical Rankine theory. Figure 5b shows that an increase in γ_g or K results in a decrease in h_{cr}. Although not presented, it is obvious from equation 8 that h_{cr} is linearly correlated with γ_g or K. Combined, these results are considered to be of considerable practical significance since a direct comparison of τ_c and τ_c^p is difficult in some cases and so a small h_{cr} is desirable. In particular, these results indicate that FO strain sensing cables of small Young's modulus and radius (known collectively as axial stiffness) are preferable in terms of ensuring a strong backfill-cable interface bond and, hence, a small h_{cr}. This also indicates a future direction for cable development during which the trade-off between robustness and interface bond should be carefully considered.

To evaluate the performance of the three cables, the influence of $[\mathrm{d}\varepsilon/\mathrm{d}z]_\mathrm{m}$ on $\sigma_{c,cr}$ and h_{cr} is investigated under typical ground and backfill-cable interface parameters (Figure 5c). As expected, larger $[\mathrm{d}\varepsilon/\mathrm{d}z]_\mathrm{m}$ values correspond to a smaller $\sigma_{c,cr}$ or h_{cr} for all the cables. For DSS-C2 and DSS-C3, $\sigma_{c,cr}$ equals 120.39 and 180.44 kPa, respectively, at a $[\mathrm{d}\varepsilon/\mathrm{d}z]_\mathrm{m}$ of 2×10^{-3} m^{-1} and zero c_c. The corresponding values of h_{cr} are 10.29 and 15.42 m, respectively. By contrast, DSS-C1 has a quite small $\sigma_{c,cr}$ of 0.82 kPa and h_{cr} of 0.07 m. With an increased c_c, the values of $\sigma_{c,cr}$ and h_{cr} can be further decreased (e.g., the case of c_c= 45 kPa in Figure 5c). Such low h_{cr} values are especially desirable in the field as this suggests that, in terms of interface bond the DSS technology can be used for deformation measurement at a near-surface environment (e.g., in a shallow trench). This again emphasizes the role of the backfill-cable interface bond that should be fully evaluated during cable development or selection.

10.1029/2019JB018878

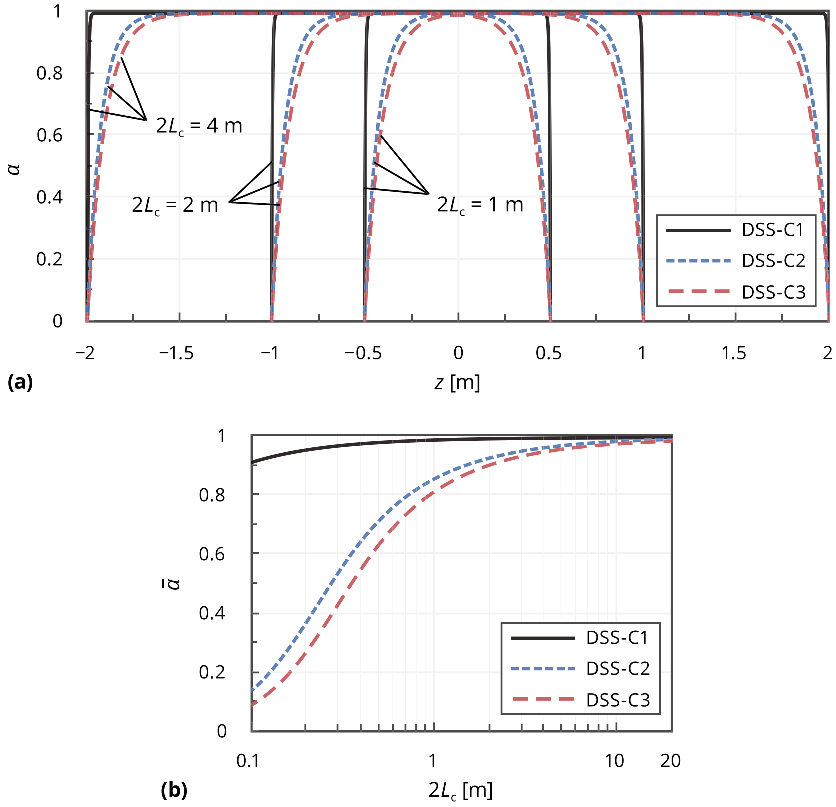

Figure 7. Gauge length dependency of ground-borehole-cable strain transfer illustrated with three fiber-optic strain sensing cables. (a) Distribution of α along cable. (b) Variation of $\bar{\alpha}$ with cable gauge length. z = distance from cable center; $2L_c$ = cable gauge length; α = ground-borehole-cable strain transfer ratio; $\bar{\alpha}$ = average strain transfer ratio over gauge length. Parameters other than those investigated are summarized in Table 2.

4.3. Parametric Analysis Results—Strain Transfer

The influence of cable, borehole, and ground property parameters on the ground-borehole-cable strain transfer efficiency is also examined through a parametric analysis and the results are presented in Figures 6–9. It is noted that most of the analysis is performed using equations 21 and 22 except for the borehole-cable interface adhesion coefficient, which can only be considered by equations 19 and 20. A summary of the parameter values employed is presented in Table 2.

From Figures 6a–6c, it may be readily observed that there is a clear, monotonic trend of decreasing $\bar{\alpha}$ with increasing cable parameter values (r_c or E_c) or decreasing borehole-cable interface adhesion coefficient (k_c). Consistent with this, the DSS-C1 cable has higher $\bar{\alpha}$ values than DSS-C2 and DSS-C3 at two simulated backfill materials (Figure 6d) and more uniform distributions of α for three gauge lengths $2L_c$ (Figure 7a). The tendency of higher L_c to improve the transfer is also seen (Figure 7b). Together with Figure 5, these results suggest that FO strain sensing cables of low axial stiffness are especially preferable in terms of both interface bond and strain transfer efficiency. Furthermore, greater gauge lengths may be recommended for cable design, which is further discussed in section 5. Notice that since the axial stiffness of DSS-C3 is of the same order of magnitude as DSS-C2 (Table 1) and their coupling properties appear to be similar to each other (Figures 6c, 6d, and 7), the analysis is focused on DSS-C1 and DSS-C2 in the remainder of the section.

The trends in $\bar{\alpha}$ resulting from variations of borehole backfill property parameters (r_b, E_b, and μ_b) and ground-borehole interface adhesion coefficient (k_b) are presented in Figure 8. $\bar{\alpha}$ decreases as r_b or μ_b increases, or as E_b decreases, indicating that boreholes of small radius and backfills of high Young's modulus or low Poisson's ratio may be preferable. Despite this, the relationship between $\bar{\alpha}$ and E_b is highly nonlinear

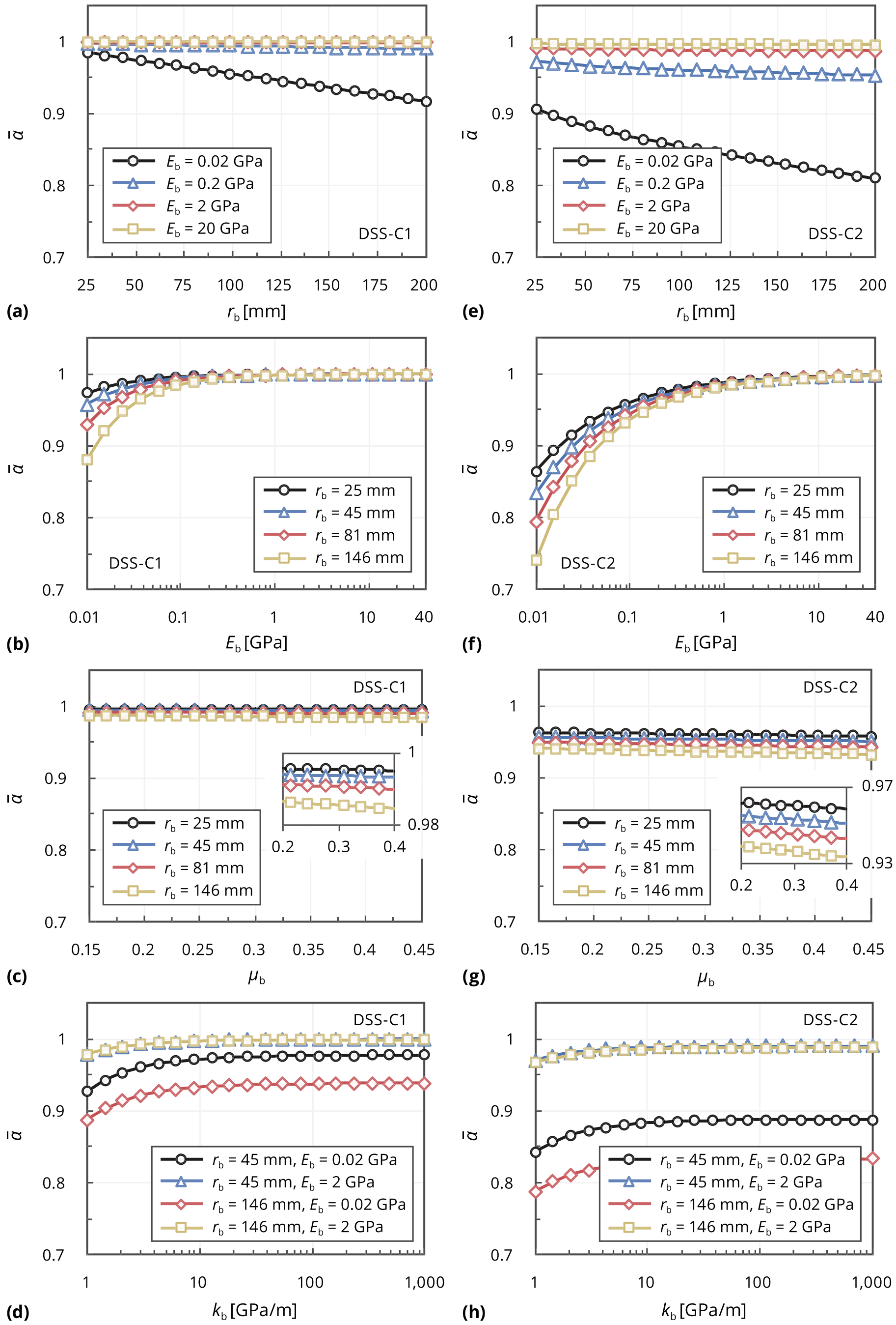

Figure 8. Effects on the average ground-borehole-cable strain transfer ratio ($\bar{\alpha}$) of variations in (a) and (e) radius of borehole (r_b); (b) and (f) Young's modulus of borehole backfill (E_b); (c) and (g) Poisson's ratio of borehole backfill (μ_b); and (d) and (h) ground-borehole interface adhesion coefficient (k_b). Parameters other than those investigated are summarized in Table 2.

for a given combination of r_b and μ_b (Figures 8b and 8f). This indicates that increasing backfill modulus may help improve strain transfer in the low modulus range, while this will likely play a limited role in the moderate to high range. By contrast, μ_b has only a slight effect on $\bar{\alpha}$ compared to r_b or E_b, though this effect is still more evident for the DSS-C2 cable than the DSS-C1 cable (Figures 8c and 8g). In addition to the influence of backfill properties, strain transfer loss may arise at low k_b, which can be further exacerbated by low E_b (Figures 8d and 8h).

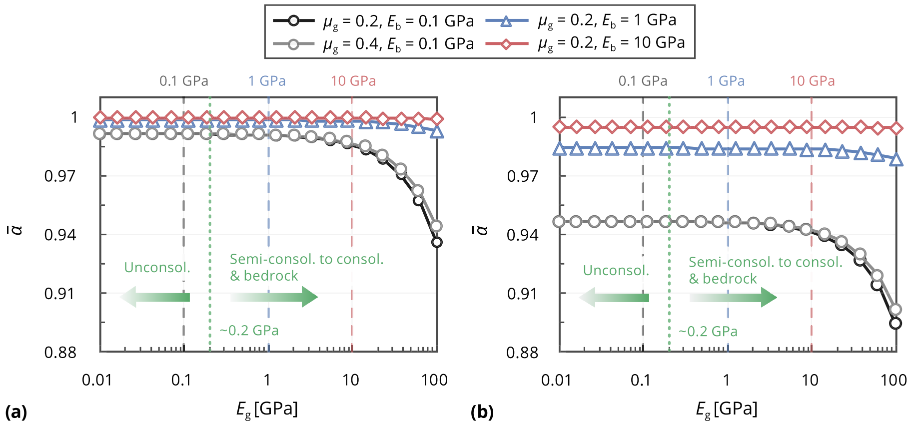

Figure 9. Effects on the average ground-borehole-cable strain transfer ratio ($\bar{\alpha}$) of variations in Young's modulus (E_g) and Poisson's ratio (μ_g) of ground for (a) DSS-C1 cable and (b) DSS-C2 cable. Green dotted line (which corresponds to a E_g of ~0.2 GPa) divides the ground modulus range: left side = unconsolidated sediments; right side = semiconsolidated to consolidated sediments and bedrock. Dashed lines denote $E_g = E_b$. The influence of μ_g is negligible at $E_b = 1$ or 10 GPa and so the results are not shown. Parameters other than those investigated are summarized in Table 2.

Figure 9 shows how the ratio $\bar{\alpha}$ correlates with ground property parameters (E_g and μ_g). It may be readily observed that $\bar{\alpha}$ is, for a given combination of E_b and μ_g, negatively correlated with E_g, but its variation with E_g is quite small for backfills of relatively high modulus (e.g., $E_b > 1$ GPa) or when $E_g < 10$ GPa (despite variation of E_b in this case). The effect of μ_g on $\bar{\alpha}$ appears to be even negligible, which is consistent with the effect of μ_b (Figures 8c and 8g). Importantly, this indicates that for strain sensing of unconsolidated sediments the effect of ground properties on strain transfer is negligible (Figure S3). With regard to semiconsolidated to consolidated sediments and rock strata, as cement-like materials of relatively high modulus are commonly employed for borehole backfilling (compared to sandy soils of low modulus for trench backfilling), the influence of ground parameter variation on strain transfer may also be neglected compared to the effects of borehole property change (Figures 8a, 8b, 8e, and 8f). As a consequence, for practical use the simplified form of equations 21 and 22 ($\chi = 1$ and so κ_2 vanishes) is brief enough yet sufficient for determining the ground-borehole-cable strain transfer efficiency.

An additional feature which may be observed from Figure 9 is that, when E_g equals E_b (see auxiliary dashed lines), there does not exist a maximum $\bar{\alpha}$ turning point. This result suggests that backfilling the borehole with that of the same modulus as the ground may not guarantee an optimal strain transfer. This likely is attributed to the influence of the ground-borehole interface effect, that is, the parameter k_b introduced in the proposed model. Furthermore, although Figure S3 suggests a slightly larger $\bar{\alpha}$ in the low E_g range, this does not indicate that soft clay strata, for example, may transfer strains efficiently to the cable as the soft clay often has a small k_b and, hence, also a relatively weak transfer (Figures 8d and 8h).

5. Recommendations

The foregoing parametric analysis shows that the ground-borehole-cable strain transfer mechanism depends strongly on the geometry and stiffness of the cable and backfill. In particular, the analysis reveals the gauge length dependency of the FO cable in transferring the strain (Figure 7). Consequently, determination of the proper gauge length, $2L_c$, for given combinations of cable and backfill property parameters is of great practical significance. Because the strain transfer ratio, α, has a dome-shaped distribution along the cable axis (Figure 7a), the gauge length required may be determined by considering that α is greater than a certain threshold, α_0, over at least half of this length (Criterion (i); Li et al., 2012), that is, $\alpha(L_c/2) \geq \alpha_0$ (e.g., α_0= 0.8, 0.9, or 0.95). Combining this inequality with equation 21 ($\chi = 1$) yields a critical gauge length, l_{crit}:

Table 2
Parameter Values Used in the Analysis of Ground-Borehole-Cable Strain Transfer

	Fiber-optic cable			Borehole				Ground				
Figure	$2L_c$ (m)	r_c (mm)	E_c (GPa)	r_b (mm)	E_b (GPa)	μ_b	k_b (GPa/m)	χ	r_g (mm)	E_g (GPa)	μ_g	k_g (GPa/m)
6a	3	0.45–4.5	1, 4, 16, 64	75	0.1	0.3	100	1.1	300	0.12	0.3	0.05
6b	3	0.5, 0.9, 1.6, 2.9	0.3–75	75	0.1	0.3	100	1.1	300	0.12	0.3	0.05
6c	3	1, 2.5, 2.9	0.37, 21.67, 28.00	75	0.1	0.3	100	—	—	—	—	—
6d	3	1, 2.5, 2.9	0.37, 21.67, 28.00	60, 120	0.06, 6	0.3	100	1.1	240, 480	0.12, 12	0.3	0.05
7	0.1–20	1, 2.5, 2.9	0.37, 21.67, 28.00	75	0.1	0.3	100	1.1	300	0.12	0.3	0.05
8a, 8e	3	1, 2.5	0.37, 21.67	25–200	0.02, 0.2, 2, 20	0.3	100	1.1	100–800	0.12	0.3	0.05
8b, 8f	3	1, 2.5	0.37, 21.67	25, 45, 81, 146	0.01–40	0.3	100	1.1	100, 180, 324, 584	0.12	0.3	0.05
8c, 8 g	3	1, 2.5	0.37, 21.67	25, 45, 81, 146	0.1	0.15–0.45	100	1.1	100, 180, 324, 584	0.12	0.3	0.05
8d, 8 h	3	1, 2.5	0.37, 21.67	45, 146	0.02, 2	0.3	1–1000	1.1	300	0.12	0.3	0.05
9	3	1, 2.5	0.37, 21.67	75	0.1, 1, 10	0.3	100	1.1	300	0.01–100	0.2, 0.4	0.05

Note. Most of the analysis is performed using equations 21 and 22 except for the borehole-cable interface adhesion coefficient, k_c, which can only be considered by equations 19 and 20. k_c varies between 0.05 and 5 GPa/m in Figure 6c. $2L_c$ = cable gauge length; r_c = cable radius; E_c = cable Young's modulus; r_b = borehole radius; E_b = backfill Young's modulus; μ_b = backfill Poisson's ratio; k_b = ground-borehole interface adhesion coefficient; χ = dimensionless model coefficient; r_g = ground radius; E_g = ground Young's modulus; μ_g = ground Poisson's ratio; k_g = surrounding ground-ground interface adhesion coefficient.

$$l_{\mathrm{crit}} = \begin{cases} \dfrac{6.58}{\lambda_2}, & \alpha_0 = 0.8 \\ \dfrac{9.25}{\lambda_2}, & \alpha_0 = 0.9 \\ \dfrac{11.99}{\lambda_2}, & \alpha_0 = 0.95 \end{cases} \tag{25}$$

Alternatively, l_{crit} may be obtained if the averaged ratio, $\bar{\alpha}$, needs to exceed α_0 (Criterion (ii)), which leads to

$$l_{\mathrm{crit}} = \begin{cases} \dfrac{10}{\lambda_2}, & \alpha_0 = 0.8 \\ \dfrac{20}{\lambda_2}, & \alpha_0 = 0.9 \\ \dfrac{40}{\lambda_2}, & \alpha_0 = 0.95 \end{cases} \tag{26}$$

From equations 25 and 26, it is evident that Criterion (ii) is more stringent than Criterion (i); selection of the criterion depends on specified design requirements. For a given combination of cable and borehole property parameters (r_c, E_c, r_b, E_b, and μ_b), λ_2 is unique and so l_{crit} can be readily calculated. The tendency of higher λ_2 to reduce l_{crit} is seen (Figure 10a). Design charts for l_{crit} versus $1/\lambda_2$ at three α_0 values are also developed following both criteria (Figures 10b and 10c).

A family of three-dimensional surface plots are presented in Figures 11 and 12. This set of plots compares the l_{crit} values of the three FO cables (DSS-C1–C3), with variations in r_b and E_b. Both the criteria and three threshold values are considered. A backfill Poisson's ratio of μ_b= 0.3 is used throughout. The trend toward a smaller l_{crit} with increasing E_b or decreasing r_b is apparent, and a higher l_{crit} needed for DSS-C2 and DSS-C3 to ensure the required transfer is clear. The value of l_{crit} for given property parameters can be found from the aforementioned design charts (Figures 10b and 10c), or more easily from appropriate design tables. An example of such tables is given in Table 3. For example, for r_b = 135 mm and E_b = 0.1 GPa the minimum gauge length required for the DSS-C1 cable is 0.18 m at a designated α_0 of 0.95 based on Criterion (ii), whereas for DSS-C2 and DSS-C3, the corresponding lengths are 3.14 and 4.05 m, respectively.

In addition to the cable gauge length described, recommendations related to the backfill modulus, E_b, are also provided. Considering the manufacturing process and cost a minimum gauge length of 1 m is considered reasonable for practical use. Given the monotonicity between model parameters, an additional analysis incorporating all parameters (including r_b, μ_b, and property parameters, r_c and E_c, of the three FO cables) would be readily performed. Results of the analysis indicate that for α_0= 0.9 (or 0.95) of Criterion (i), a E_b of 0.11 GPa (respectively, 0.18 GPa) would be sufficient to achieve the desired transfer despite variation of other parameters. With regard to Criterion (ii), the corresponding values of E_b are 0.51 and 2.04 GPa, respectively. Furthermore, the critical value of backfill modulus, $E_{b,\mathrm{crit}}$, satisfying a designated α_0 is as follows:

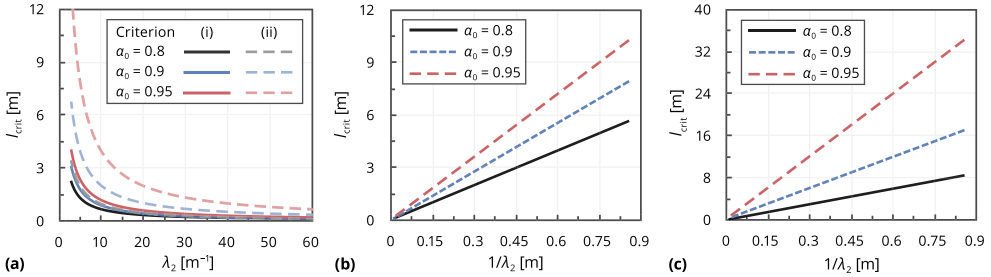

Figure 10. (a) Correlation of cable critical gauge length (l_{crit}) with variation in λ_2 at three strain transfer threshold (α_0) values following two different criteria. Design charts for l_{crit} versus $1/\lambda_2$ following (b) Criteria (i) and (c) Criteria (ii). λ_2 = parameter encapsulating the effects of cable radius (r_c) and modulus (E_c), borehole radius (r_b), and backfill modulus (E_b) and Poisson's ratio (μ_b).

$$E_{\mathrm{b,crit}} = E_c r_c^2 (1+\mu_b)\left(\frac{r_b^2}{r_b^2-r_c^2}\ln\frac{r_b}{r_c}-\frac{1}{2}\right)\left(\frac{i}{2L}\right)^2 \tag{27}$$

where i is correlated with α_0 (Criterion (i)):

$$i = \begin{cases} 6.58, & \alpha_0 = 0.8 \\ 9.25, & \alpha_0 = 0.9 \\ 11.99, & \alpha_0 = 0.95 \end{cases} \tag{28}$$

or under Criterion (ii) i is given by

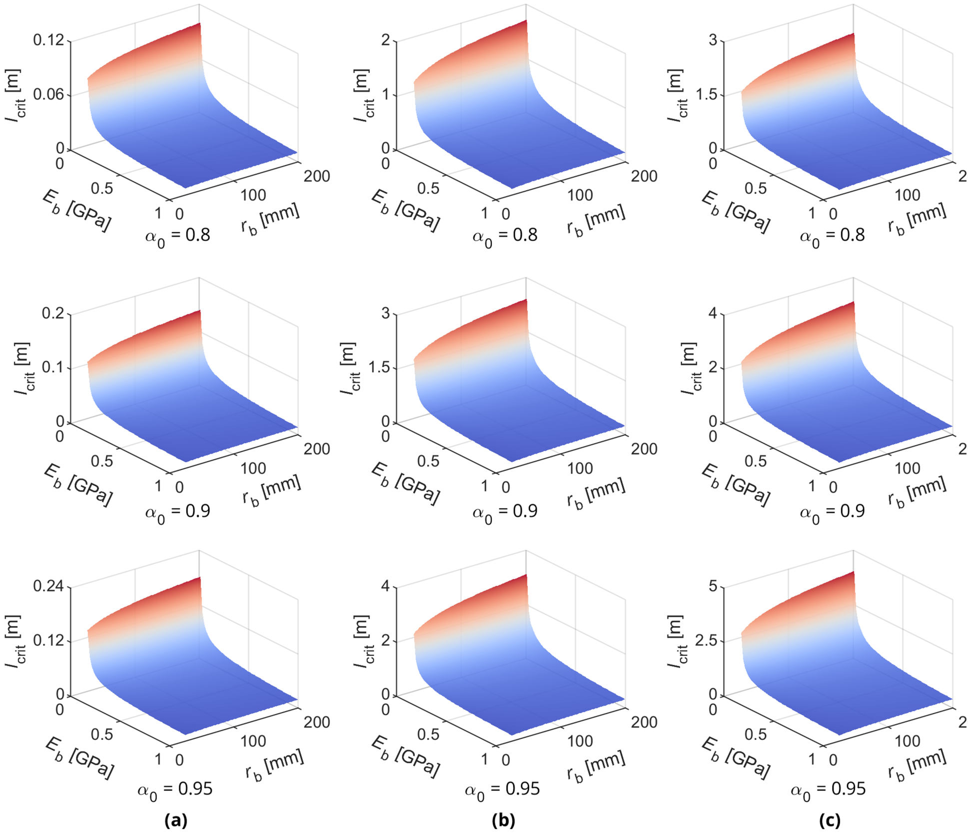

Figure 11. Plots of critical gauge length (l_{crit}) as functions of borehole radius (r_b) and backfill modulus (E_b) at three threshold values of strain transfer ratio (α_0) following Criterion (i) for three fiber-optic cables: (a) DSS-C1; (b) DSS-C2; and (c) DSS-C3. A modulus range from 0.01 to 1 GPa is employed as the average strain transfer ratio is greater than 0.95 for higher modulus values. The Poisson's ratio of backfill, μ_b= 0.3, is held constant.

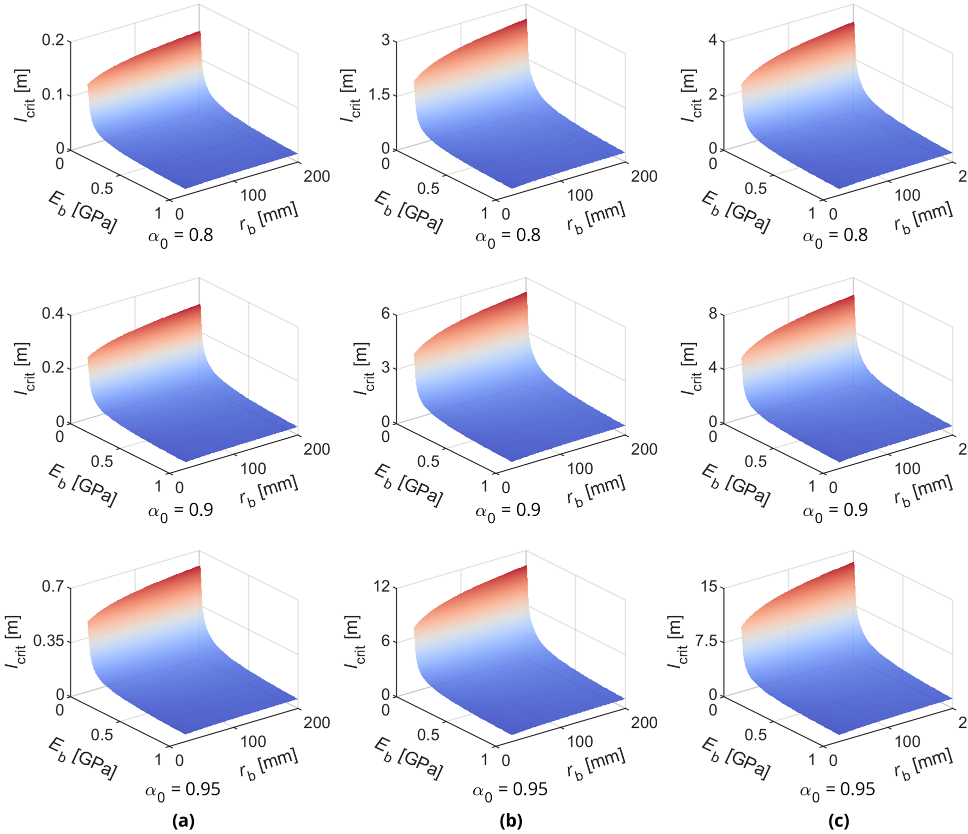

Figure 12. Plots of critical gauge length (l_{crit}) as functions of borehole radius (r_{b}) and backfill modulus (E_{b}) at three threshold values of strain transfer ratio (α_0) following Criterion (ii) for three fiber-optic cables: (a) DSS-C1; (b) DSS-C2; and (c) DSS-C3. A modulus range from 0.01 to 1 GPa is employed as the average strain transfer ratio is greater than 0.95 for higher modulus values. The Poisson's ratio of backfill, μ_{b}= 0.3, is held constant.

$$i = \begin{cases} 10, & \alpha_0 = 0.8 \\ 20, & \alpha_0 = 0.9 \\ 40, & \alpha_0 = 0.95 \end{cases} \tag{29}$$

According to equations 27–29, a design table for backfill modulus is also developed and presented in Table 4.

6. Discussion

We have proposed a theoretical method for evaluating quantitatively the mechanical coupling between a buried FO cable and its surroundings when the DSS technology is employed to record Earth materials deformation. Previous coupling studies (e.g., Iten et al., 2009; Zhang et al., 2016) have primarily focused on the ground-cable interface shear failure criterion (ASTM F3079-14, 2014), which does not allow to recover the actual amount of deformation from fiber optics-measured strains. By contrast, our approach presented herein considers both the interface shear failure and the efficiency of strain transfer from ground to cable and thus allows the quantification of how much of the ground movement-induced strain is transferred to the sensing element through interface shear.

Strain gradient derived from measured FO strains associated with ground deformation pattern is a key parameter determining the ground-cable interface bond (equations 5 and 7). A maximum strain gradient of 2×10^{-3} m^{-1} constrained using the Shengze fiber strain data set, together with typical other parameter values, yields critical confining pressure and depth values for the three FO strain sensing cables investigated (Figure 5c). These reference values may or may not be applicable to other DSS field experiments; the strain gradient range depends on geological contexts and deformation scenarios. For ground-cable strain transfer

Table 3
A Design Table for Critical Gauge Length (l_{crit}) of Three Fiber-Optic Strain Sensing Cables (DSS-C1–C3)

			DSS-C1			DSS-C2			DSS-C3		
			E_b (GPa)			E_b (GPa)			E_b (GPa)		
			0.01	0.1	1	0.01	0.1	1	0.01	0.1	1
Criterion	α_0	r_b (mm)	l_{crit} (m)			l_{crit} (m)			l_{crit} (m)		
(i)	0.8	45	0.08	0.03	0.01	1.35	0.43	0.14	1.73	0.55	0.17
		90	0.09	0.03	0.01	1.53	0.49	0.15	1.97	0.62	0.20
		135	0.10	0.03	0.01	1.63	0.52	0.16	2.10	0.67	0.21
		180	0.10	0.03	0.01	1.70	0.54	0.17	2.19	0.69	0.22
	0.9	45	0.12	0.04	0.01	1.90	0.60	0.19	2.43	0.77	0.24
		90	0.13	0.04	0.01	2.16	0.68	0.22	2.77	0.88	0.28
		135	0.13	0.04	0.01	2.29	0.73	0.23	2.96	0.94	0.30
		180	0.14	0.04	0.01	2.39	0.75	0.24	3.08	0.97	0.31
	0.95	45	0.15	0.05	0.02	2.46	0.78	0.25	3.15	1.00	0.31
		90	0.17	0.05	0.02	2.79	0.88	0.28	3.60	1.14	0.36
		135	0.17	0.06	0.02	2.97	0.94	0.30	3.84	1.21	0.38
		180	0.18	0.06	0.02	3.09	0.98	0.31	4.00	1.26	0.40
(ii)	0.8	45	0.13	0.04	0.01	2.06	0.65	0.21	2.63	0.83	0.26
		90	0.14	0.04	0.01	2.33	0.74	0.23	3.00	0.95	0.30
		135	0.15	0.05	0.01	2.48	0.78	0.25	3.20	1.01	0.32
		180	0.15	0.05	0.02	2.58	0.82	0.26	3.33	1.05	0.33
	0.9	45	0.25	0.08	0.03	4.11	1.30	0.41	5.25	1.66	0.53
		90	0.28	0.09	0.03	4.66	1.47	0.47	6.00	1.90	0.60
		135	0.29	0.09	0.03	4.96	1.57	0.50	6.40	2.02	0.64
		180	0.30	0.10	0.03	5.16	1.63	0.52	6.67	2.11	0.67
	0.95	45	0.50	0.16	0.05	8.22	2.60	0.82	10.51	3.32	1.05
		90	0.55	0.18	0.06	9.32	2.95	0.93	12.00	3.79	1.20
		135	0.58	0.18	0.06	9.92	3.14	0.99	12.79	4.05	1.28
		180	0.60	0.19	0.06	10.32	3.26	1.03	13.33	4.22	1.33

Note. A backfill Poisson's ratio of $\mu_b = 0.3$ is used throughout. α_0 = strain transfer ratio threshold; r_b = borehole radius; E_b = backfill Young's modulus. See Table 1 for descriptions of the three cables.

analysis we consider a fixed-point or microanchored design (Figure S1), which has become increasingly popular for DSS applications (Hauswirth et al., 2012; Iten et al., 2011; Picarelli et al., 2015; Schenato et al., 2017). We treat each cable section (separated by two neighboring anchor-like elements) separately and assume an axially uniform strain field within each section. The resulting strain transfer function has a concise hyperbolic form (equations 19–22) and is thus easy to implement in practice. The transfer of an arbitrary strain field from host material to fiber was addressed using Fourier decomposition and transform (Duck & LeBlanc, 2000); however, the spatial-varying nature of geomechanical deformation might hinder its application to large-scale field monitoring campaigns.

According to our calculations, a sufficient strain transfer from surrounding formations to an FO cable can be expected if the cable is installed in a vertical borehole and in the case of a cement-like backfill of relatively high modulus (Figure 9). By contrast, in cases where the cable is trenched at the near surface, ground-cable strain transfer loss may arise for trenches of large dimensions (high r_b; Figures 8a and 8e), which can be exacerbated by soil backfills that are insufficiently tamped (low E_b; Figures 8b and 8f). Moreover, the low confining pressure exerted on the soil-cable interface for horizontally trenched direct burial may increase the possibility of interface slippage, especially for a high strain gradient present in the ground.

The limit on SR of an FO interrogator is yet another source of error in distributed strain measurements. Due to this optoelectronic effect the measured strain profile is a weighted average of the true strain over a length equivalent to the interrogator SR. The SR of Brillouin scattering-based devices popularized in DSS applications is in meters or submeters (Sasaki et al., 2019; Zhang et al., 2018). Rayleigh-based OFDR (Kwon et al., 2018; Lanticq et al., 2009; Schenato et al., 2017) and TW-COTDR (Kogure & Okuda, 2018; Zhang &

Table 4
A Design Table for Critical Backfill Modulus ($E_{b,crit}$)

			DSS-C1				DSS-C2				DSS-C3			
			$2L_c$ (m)				$2L_c$ (m)				$2L_c$ (m)			
			1	2	5	10	1	2	5	10	1	2	5	10
Criterion	α_0	r_b (mm)	$E_{b,crit}$ (MPa)				$E_{b,crit}$ (MPa)				$E_{b,crit}$ (MPa)			
(i)	0.8	45	0.07	0.02	—	—	18.29	4.57	0.73	0.18	29.87	7.47	1.19	0.30
		90	0.08	0.02	—	—	23.53	5.88	0.94	0.24	38.95	9.74	1.56	0.39
		135	0.09	0.02	—	—	26.61	6.65	1.06	0.27	44.30	11.07	1.77	0.44
		180	0.10	0.02	—	—	28.80	7.20	1.15	0.29	48.10	12.03	1.92	0.48
	0.9	45	0.14	0.03	0.01	—	36.15	9.04	1.45	0.36	59.02	14.76	2.36	0.59
		90	0.16	0.04	0.01	—	46.49	11.62	1.86	0.46	76.97	19.24	3.08	0.77
		135	0.18	0.05	0.01	—	52.58	13.15	2.10	0.53	87.54	21.89	3.50	0.88
		180	0.19	0.05	0.01	—	56.91	14.23	2.28	0.57	95.06	23.77	3.80	0.95
	0.95	45	0.23	0.06	0.01	—	60.73	15.18	2.43	0.61	99.17	24.79	3.97	0.99
		90	0.28	0.07	0.01	—	78.12	19.53	3.12	0.78	129.33	32.33	5.17	1.29
		135	0.30	0.08	0.01	—	88.35	22.09	3.53	0.88	147.09	36.77	5.88	1.47
		180	0.32	0.08	0.01	—	95.61	23.90	3.82	0.96	159.72	39.93	6.39	1.60
(ii)	0.8	45	0.16	0.04	0.01	—	42.24	10.56	1.69	0.42	68.98	17.25	2.76	0.69
		90	0.19	0.05	0.01	—	54.34	13.58	2.17	0.54	89.96	22.49	3.60	0.90
		135	0.21	0.05	0.01	—	61.45	15.36	2.46	0.61	102.32	25.58	4.09	1.02
		180	0.23	0.06	0.01	—	66.51	16.63	2.66	0.67	111.10	27.78	4.44	1.11
	0.9	45	0.64	0.16	0.03	0.01	168.98	42.24	6.76	1.69	275.93	68.98	11.04	2.76
		90	0.77	0.19	0.03	0.01	217.36	54.34	8.69	2.17	359.84	89.96	14.39	3.60
		135	0.85	0.21	0.03	0.01	245.82	61.45	9.83	2.46	409.27	102.32	16.37	4.09
		180	0.90	0.23	0.04	0.01	266.04	66.51	10.64	2.66	444.41	111.10	17.78	4.44
	0.95	45	2.55	0.64	0.10	0.03	675.91	168.98	27.04	6.76	1103.71	275.93	44.15	11.04
		90	3.08	0.77	0.12	0.03	869.44	217.36	34.78	8.69	1439.36	359.84	57.57	14.39
		135	3.39	0.85	0.14	0.03	983.27	245.82	39.33	9.83	1637.07	409.27	65.48	16.37
		180	3.61	0.90	0.14	0.04	1064.16	266.04	42.57	10.64	1777.63	444.41	71.11	17.78

Note. For presentation purposes the unit of MPa is used for modulus values in this table. "—" indicates modulus bellow 0.01 MPa. A backfill Poisson's ratio of $\mu_b = 0.3$ is used throughout. α_0 = strain transfer ratio threshold; r_b = borehole radius; $2L_c$ = cable gauge length. See Table 1 for descriptions of the three cables.

Xue, 2019) have higher spatial resolutions (millimeters and centimeters, respectively), compromising the measurement distance. Evidence suggested that the cable mechanical transfer function and the interrogator SR jointly determined the effective SR of a DSS system (Henault et al., 2012). Specifically, analysis of a Dirac strain distribution associated with fissure detection showed that the DSS system effective SR was controlled to a first order by the interrogator SR for a full width at half maximum of 10 cm of the transfer function and an interrogator SR of 1 m. On the contrary, the system performance was affected primarily by strain transfer if the interrogator SR was reduced down to 1 cm. This implies that ground-fiber strain transfer analyses can recover true ground deformation values given a high interrogator SR (e.g., centimeters or less as assumed by Buchoud et al., 2016), while an additional quantification of the SR effect would be necessary if the SR is limited (particularly for BOTDR commonly used in DSS studies). However, the exact limit of high and low SRs pertaining to ground deformation measurement requires future research. Furthermore, anchor-like elements mechanically attached to an FO cable can improve the ground-cable interface shear strength (Hauswirth et al., 2012), but may result in a reduction in the effective SR if the anchor interval (here termed gauge length) is larger than the interrogator SR (Schenato, 2017). This effect further complicates actual ground deformation recovery. We conclude that future evaluation of the coupled effects of ground-fiber coupling, interrogator SR, and anchorage is necessary to retrieve more accurate distributed strain profiles of the subsurface.

7. Conclusions

DSS, coupled with subsurface FO cables, is enabling distributed sensing of ground deformation. However, strain signatures acquired directly with an FO cable is not entirely representative of those induced in the ground, mainly due to unquantified fiber sensing element response related to the ground-fiber coupling effect. In this study, we present a theoretical investigation of the interaction and interface shear transfer of a ground-borehole-cable system, following a two-step coupling evaluation procedure developed for DSS. We carry out extensive parametric analyses of ground-borehole-cable interface bond and strain transfer, with particular emphasis on the performance of three archetypal strain sensing cables.

The critical confining pressure and the critical depth, proposed to characterize the ground-cable interface bond, correlate positively with maximum strain gradient and cable radius and modulus (or equivalently cable axial stiffness), while being negatively correlated with ground weight density, lateral Earth pressure coefficient, and interface friction angle and cohesion. The quality of ground-borehole-cable strain transfer increases with increasing cable gauge length and backfill modulus or decreasing cable axial stiffness and borehole radius while being comparably insensitive to variations in ground property parameters. Hence, FO cables of low axial stiffness may be preferred in terms of both interface bond and strain transfer, provided they are capable of withstanding the impacts associated with installation and of operating in harsh geoenvironmental conditions. Design charts and tables developed at designated transfer ratios may further facilitate cable development and field deployment. Furthermore, the simplified expression for the ground-borehole-cable strain transfer ratio (equation 22 with $\chi = 1$) is brief yet useful for approximating the ground-to-cable strain transfer efficiency, requiring only geometry and modulus values of the cable and backfill.

Future work is needed to elucidate the effect of SR on recorded DSS data relative to the coupling effect presently analyzed. Quantification of both fiber sensing element response and optoelectronic system response will allow the measurement of distributed subsurface strain profiles with higher accuracy.

Appendix A: Derivation of Governing Equations for Ground-Borehole-Cable Strain Transfer

A1. Consideration of Borehole-Cable Interface Property

Assuming a linear stress-displacement constitutive relation holds for both the borehole-cable and ground-borehole interfaces, we have

$$\tau_\mathrm{c}(z, r_\mathrm{c}) = k_\mathrm{c} \Delta u_\mathrm{c} \tag{A1}$$

$$\tau_\mathrm{b}(z, r_\mathrm{b}) = k_\mathrm{b} \Delta u_\mathrm{b} \tag{A2}$$

where k_c is the borehole-cable interface adhesion coefficient and k_b is the ground-borehole interface adhesion coefficient.

Combining equation A1 with equations 10 and 15, $\partial \sigma_\mathrm{b} / \partial z$ is written in terms of $\partial \sigma_\mathrm{c} / \partial z$ as

$$\frac{\partial \sigma_\mathrm{b}(z)}{\partial z} = \frac{\frac{r_\mathrm{c}}{2} - \frac{k_\mathrm{c}}{G_\mathrm{b}} \frac{r_\mathrm{c}^2}{2} \ln \frac{r_\mathrm{b}}{r_\mathrm{c}}}{\frac{k_\mathrm{c}}{G_\mathrm{b}} \left(\frac{r_\mathrm{b}^2 - r_\mathrm{c}^2}{4} - \frac{r_\mathrm{c}^2}{2} \ln \frac{r_\mathrm{b}}{r_\mathrm{c}} \right)} \frac{\partial \sigma_\mathrm{c}(z)}{\partial z} \tag{A3}$$

Using this and combining equation A2 with equations 11 and 16, $\partial \sigma_\mathrm{g} / \partial z$ is expressed as

$$\frac{\partial \sigma_\mathrm{g}(z)}{\partial z} = \frac{\dfrac{\dfrac{r_\mathrm{c}}{2} - \dfrac{k_\mathrm{c} r_\mathrm{c}^2}{G_\mathrm{b}\, 2} \ln \dfrac{r_\mathrm{b}}{r_\mathrm{c}}}{\dfrac{k_\mathrm{c}}{G_\mathrm{b}} \left(\dfrac{r_\mathrm{b}^2 - r_\mathrm{c}^2}{4} - \dfrac{r_\mathrm{c}^2}{2} \ln \dfrac{r_\mathrm{b}}{r_\mathrm{c}} \right)} \left(\dfrac{r_\mathrm{b}^2 - r_\mathrm{c}^2}{2 r_\mathrm{b}} - \dfrac{k_\mathrm{b}}{G_\mathrm{g}} \ln \dfrac{r_\mathrm{g}}{r_\mathrm{b}} \dfrac{r_\mathrm{b}^2 - r_\mathrm{c}^2}{2} \right) + \dfrac{r_\mathrm{c}^2}{2 r_\mathrm{b}} - \dfrac{k_\mathrm{b}}{G_\mathrm{g}} \ln \dfrac{r_\mathrm{g}}{r_\mathrm{b}} \dfrac{r_\mathrm{c}^2}{2}}{\dfrac{k_\mathrm{b}}{G_\mathrm{g}} \left(\dfrac{r_\mathrm{g}^2 - r_\mathrm{b}^2}{4} - \dfrac{r_\mathrm{b}^2}{2} \ln \dfrac{r_\mathrm{g}}{r_\mathrm{b}} \right)} \frac{\partial \sigma_\mathrm{c}(z)}{\partial z} \tag{A4}$$

Using these results and combining equation 15 with equation 16, we arrive at

$$\left[\frac{r_c}{2k_c}+\frac{r_c^2}{2k_b r_b}+\frac{\left(r_b^2-r_c^2\right)\left(\frac{r_c}{2}-\frac{k_c}{G_b}\frac{r_c^2}{2}\ln\frac{r_b}{r_c}\right)}{\frac{2k_b r_b k_c}{G_b}\left(\frac{r_b^2-r_c^2}{4}-\frac{r_c^2}{2}\ln\frac{r_b}{r_c}\right)}\right]\frac{\partial\sigma_c(z)}{\partial z}-u_c=-u_g \tag{A5}$$

Equation A5 is differentiated with respect to z yielding

$$\frac{1}{\lambda_1^2}\varepsilon_c{}''-\varepsilon_c=-\varepsilon_g \tag{A6}$$

where λ_1 is a parameter encapsulating the effects of geometry and modulus of the cable and backfill and the adhesion coefficients of the interfaces. By employing $G = E/2(1+\mu)$, λ_1 is written as

$$\lambda_1=\left[\frac{E_c r_c}{2k_c}+\frac{E_c r_c^2}{2k_b r_b}+\frac{E_c\left(r_b^2-r_c^2\right)\left(E_b r_c-2(1+\mu_b)k_c r_c^2\ln\frac{r_b}{r_c}\right)}{2k_b k_c r_b(1+\mu_b)\left(r_b^2-r_c^2-2r_c^2\ln\frac{r_b}{r_c}\right)}\right]^{-\frac{1}{2}} \tag{A7}$$

Here we consider a fixed-point or microanchored design for the cable (with a gauge length of $2L_c$; Figure S1) and assume that the ground strain is uniform within this length, then we have

$$\varepsilon_g(z=\pm L_c)=0 \tag{A8}$$

$$\overline{\varepsilon_g}=\frac{1}{2L_c}\int_{-L_c}^{L_c}\varepsilon_g(z)\mathrm{d}z \tag{A9}$$

Finally, the solution to the second-order linear differential equation, equation A6, with the boundary conditions, equation A9, is in a concise form:

$$\varepsilon_c=\left(1-\frac{\cosh(\lambda_1 z)}{\cosh(\lambda_1 L_c)}\right)\overline{\varepsilon_g} \tag{A10}$$

Define a ratio, α, quantifying the strain transfer from the ground to the cable, $\alpha=\varepsilon_c/\overline{\varepsilon_g}$. Over the gauge length, the average strain transfer ratio, $\overline{\alpha}$, is readily obtained as

$$\overline{\alpha}=1-\frac{\tanh(\lambda_1 L_c)}{\lambda_1 L_c} \tag{A11}$$

A2. Consideration of Ground Property

To consider the effects of ground properties on the ground-borehole-cable strain transfer efficiency, the linear stress-displacement constitutive relation is, again, introduced for the interface between the surrounding ground and the ground under consideration:

$$\tau_g\left(z,r_g\right)=k_g\Delta u_g \tag{B1}$$

where k_g is the adhesion coefficient for the interface between the surrounding ground and the ground under consideration and Δu_g is the relative displacement between the two components, which is assumed to satisfy

$$u_g+\Delta u_g=\chi u_g \tag{B2}$$

where χ is a dimensionless coefficient quantifying the effects of ground parameters on the strain transfer property.

Similarly as in the derivation of equation A5, the expression for $\partial\sigma_g/\partial z$ is obtained by combining equation A2 with equations 11 and 16. Now $\partial\sigma_b/\partial z$ is sought by substitution of equations B2 and B1 into equation 12. These lead to the following governing equation (Xiang & Wang, 2018):

$$\frac{1}{\lambda_2^2}\varepsilon_c{}'' - \varepsilon_c = -\kappa_2\overline{\varepsilon_g} \tag{B3}$$

where λ_2 and κ_2 have the following forms:

$$\lambda_2 = \left[\frac{E_c}{E_b} r_c^2 (1+\mu_b)\left(\frac{r_b^2}{r_b^2 - r_c^2}\ln\frac{r_b}{r_c} - \frac{1}{2}\right)\right]^{-\frac{1}{2}} \tag{B4}$$

$$\begin{aligned}\kappa_2 = 1 - &\frac{(\chi-1)k_g r_g\left(\ln\frac{r_g}{r_b} - \frac{E_g}{2k_b r_b\left(1+\mu_g\right)}\right)}{\frac{r_g^2 - r_b^2}{4} - \frac{r_g^2}{2}\ln\frac{r_g}{r_b} + \frac{\left(1+\mu_g\right)\left(r_g^2 - r_b^2\right)}{k_b r_b E_g}}\cdot\\ &\left[\frac{(1+\mu_b)\left(r_g^2 - r_b^2\right)}{E_b}\left(\frac{1}{4} - \frac{r_c^2}{2\left(r_b^2 - r_c^2\right)}\ln\frac{r_b}{r_c}\right) + \frac{1+\mu_g}{E_g}\left(r_g^2\ln\frac{r_g}{r_b} - \frac{r_g^2 - r_b^2}{2}\right)\right]\\ &-2(\chi-1)k_g r_g\left[\frac{1+\mu_g}{E_g}\ln\frac{r_g}{r_b} + \frac{1+\mu_b}{E_b}\left(\frac{1}{2} - \frac{r_c^2}{r_b^2 - r_c^2}\ln\frac{r_b}{r_c}\right)\right]\end{aligned} \tag{B5}$$

Finally, considering the boundary conditions (equation A9), we get

$$\alpha = \kappa_2\left(1 - \frac{\cosh(\lambda_2 z)}{\cosh(\lambda_2 L_c)}\right) \tag{B6}$$

and therefore

$$\overline{\alpha} = \kappa_2\left(1 - \frac{\tanh(\lambda_2 L_c)}{\lambda_2 L_c}\right) \tag{B7}$$

Acknowledgments

We thank H.-R. Jiao and X. Zheng for determining cable parameters, Z.-W. Ding for helpful discussions on an earlier version of this article, and two anonymous reviewers for their constructive feedback. This work was supported by the National Natural Science Foundation of China (NSFC) Grants 41427801 and 41230636 to B. S. and a fellowship from the China Scholarship Council Grant 201706190165 to C.-C. Z. H.-H. Z. was supported by the National Key R&D Program of China Grant 2018YFC1505104 and NSFC Grant 41722209. Data to support this research are available on repository (doi: 10.6084/m9.figshare.11521872).

References

Amoruso, A., Crescentini, L., Scarpa, R., Bilham, R., Linde, A. T., & Sacks, I. S. (2015). Abrupt magma chamber contraction and microseismicity at Campi Flegrei, Italy: Cause and effect determined from strainmeters and tiltmeters. *Journal of Geophysical Research: Solid Earth*, *120*, 5467–5478. https://doi.org/10.1002/2015JB012085

Ansari, F., & Yuan, L. (1998). Mechanics of bond and interface shear transfer in optical fiber sensors. *Journal of Engineering Mechanics*, *124*(4), 385–394. https://doi.org/10.1061/(ASCE)0733-9399(1998)124:4(385)

ASTM F3079-14 (2014). Standard practice for use of distributed optical fiber sensing systems for monitoring the impact of ground movements during tunnel and utility construction on existing underground utilities. West Conshohocken, PA, United States: ASTM International. https://doi.org/10.1520/F3079-14

Bao, X., & Chen, L. (2012). Recent progress in distributed fiber optic sensors. *Sensors*, *12*(7), 8601–8639. https://doi.org/10.3390/s120708601

Barbour, A. J., Evans, E. L., Hickman, S. H., & Eneva, M. (2016). Subsidence rates at the southern Salton Sea consistent with reservoir depletion. *Journal of Geophysical Research: Solid Earth*, *121*, 5308–5327. https://doi.org/10.1002/2016JB012903

Brenguier, F., Shapiro, N. M., Campillo, M., Ferrazzini, V., Duputel, Z., Coutant, O., & Nercessian, A. (2008). Towards forecasting volcanic eruptions using seismic noise. *Nature Geoscience*, *1*(2), 126–130. https://doi.org/10.1038/ngeo104

Buchoud, E., Vrabie, V., Mars, J. I., D'Urso, G., Girard, A., Blairon, S., & Henault, J.-M. (2016). Quantification of submillimeter displacements by distributed optical fiber sensors. *IEEE Transactions on Instrumentation and Measurement*, *65*(2), 413–422. https://doi.org/10.1109/TIM.2015.2485340

Denchik, N., Gautier, S., Dupuy, M., Batiot-Guilhe, C., Lopez, M., Léonardi, V., et al. (2019). In-situ geophysical and hydro-geochemical monitoring to infer landslide dynamics (Pégairolles-de-l'Escalette landslide, France). *Engineering Geology*, *254*, 102–112. https://doi.org/10.1016/j.enggeo.2019.04.009

Duck, G., & LeBlanc, M. (2000). Arbitrary strain transfer from a host to an embedded fiber-optic sensor. *Smart Materials and Structures*, *9*(4), 492–497. https://doi.org/10.1088/0964-1726/9/4/312

Erban, L. E., Gorelick, S. M., Zebker, H. A., & Fendorf, S. (2013). Release of arsenic to deep groundwater in the Mekong Delta, Vietnam, linked to pumping-induced land subsidence. *Proceedings of the National Academy of Sciences*, *110*(34), 13,751–13,756. https://doi.org/10.1073/pnas.1300503110

Fan, X., Scaringi, G., Korup, O., West, A. J., Westen, C. J., Tanyas, H., et al. (2019). Earthquake-induced chains of geologic hazards: Patterns, mechanisms, and impacts. *Reviews of Geophysics*, *57*, 421–503. https://doi.org/10.1029/2018RG000626

Galloway, D. L., & Burbey, T. J. (2011). Review: Regional land subsidence accompanying groundwater extraction. *Hydrogeology Journal*, *19*(8), 1459–1486. https://doi.org/10.1007/s10040-011-0775-5

Habel, W. R., & Krebber, K. (2011). Fiber-optic sensor applications in civil and geotechnical engineering. *Photonic Sensors*, *1*(3), 268–280. https://doi.org/10.1007/s13320-011-0011-x

Hartog, A. H. (2017). *An introduction to distributed optical fibre sensors* (1st ed.). Boca Raton, FL: CRC Press. https://doi.org/10.1201/9781315119014

Hauswirth, D., Iten, M., & Puzrin, A. M. (2012). Detection of ground movements using soil-embedded distributed fiber optic sensors. In R. Q. Coutinho & P. W. Mayne (Eds.), *Geotechnical and geophysical site characterization 4* (pp. 579–586). London, UK: CRC Press. https://doi.org/10.1201/b13251-68

Henault, J. M., Salin, J., Moreau, G., Quiertant, M., Taillade, F., Benzarti, K., & Delepine-Lesoille, S. (2012). Analysis of the strain transfer mechanism between a truly distributed optical fiber sensor and the surrounding medium. In M. G. Alexander, H.-D. Beushausen, F. Dehn, & P. Moyo (Eds.), *Concrete repair, rehabilitation and retrofitting III—Proceedings of the 3rd International Conference on Concrete Repair, Rehabilitation and Retrofitting, ICCRRR-3, 3–5 September 2012, Cape Town, South Africa* (pp. 733–739). London, UK: CRC Press.

Horiguchi, T., Kurashima, T., & Tateda, M. (1989). Tensile strain dependence of Brillouin frequency shift in silica optical fibers. *IEEE Photonics Technology Letters*, *1*(5), 107–108. https://doi.org/10.1109/68.34756

Huntley, D., Bobrowsky, P., Hendry, M., Macciotta, R., Elwood, D., Sattler, K., et al. (2019). Application of multi-dimensional electrical resistivity tomography datasets to investigate a very slow-moving landslide near Ashcroft, British Columbia, Canada. *Landslides*, *16*(5), 1033–1042. https://doi.org/10.1007/s10346-019-01147-1

Iten, M., Hauswirth, D., & Puzrin, A. M. (2011). Distributed fiber optic sensor development, testing, and evaluation for geotechnical monitoring applications. In W. Ecke, K. J. Peters, & T. E. Matikas (Eds.), *Proc. SPIE 7982, Smart sensor phenomena, technology, networks, and systems 2011* (p. 798207). San Diego, CA: SPIE. https://doi.org/10.1117/12.881228

Iten, M., Puzrin, A. M., Hauswirth, D., Foaleng-Mafang, S., Beugnot, J.-C., & Thévenaz, L. (2009). Study of a progressive failure in soil using BEDS. In J. D. C. Jones (Ed.), Proc. SPIE 7503, 20th International Conference on Optical Fibre Sensors (p. 75037S). https://doi.org/10.1117/12.835115

Iten, M., Puzrin, A. M., & Schmid, A. (2008). Landslide monitoring using a road-embedded optical fiber sensor. In W. Ecke, K. J. Peters, & N. G. Meyendorf (Eds.), Proc. SPIE 6933, Smart Sensor Phenomena, Technology, Networks, and Systems (Vol. 6933, pp. 693,315–693,319). San Diego, CA: SPIE. https://doi.org/10.1117/12.774515

Kogure, T., & Okuda, Y. (2018). Monitoring the vertical distribution of rainfall-induced strain changes in a landslide measured by distributed fiber optic sensing with Rayleigh backscattering. *Geophysical Research Letters*, *45*, 4033–4040. https://doi.org/10.1029/2018GL077607

Kwon, Y.-S., Seo, D.-C., Choi, B.-H., Jeon, M., & Kwon, I.-B. (2018). Strain measurement distributed on a ground anchor bearing plate by fiber optic OFDR sensor. *Applied Sciences*, *8*(11), 2051. https://doi.org/10.3390/app8112051

Lanticq, V., Bourgeois, E., Magnien, P., Dieleman, L., Vinceslas, G., Sang, A., & Delepine-Lesoille, S. (2009). Soil-embedded optical fiber sensing cable interrogated by Brillouin optical time-domain reflectometry (B-OTDR) and optical frequency-domain reflectometry (OFDR) for embedded cavity detection and sinkhole warning system. *Measurement Science and Technology*, *20*(3), 034018. https://doi.org/10.1088/0957-0233/20/3/034018

LeBlanc, M. (1999). *Interaction mechanics of embedded single-ended optical fibre sensors using novel in-situ measurement techniques*. Canada: University of Toronto.

Lellouch, A., Yuan, S., Spica, Z., Biondi, B., & Ellsworth, W. L. (2019). Seismic velocity estimation using passive downhole distributed acoustic sensing records: Examples from the San Andreas Fault Observatory at Depth. *Journal of Geophysical Research: Solid Earth*, *124*, 6931–6948. https://doi.org/10.1029/2019JB017533

Li, D., Ren, L., & Li, H. (2012). Mechanical property and strain transferring mechanism in optical fiber sensors. In M. Yasin, S. W. Harun, & H. Arof (Eds.), *Fiber optic sensors* (pp. 439–458). Rijeka, Croatia: INTECH. https://doi.org/10.5772/27731

Li, H.-N., Zhou, G., Ren, L., & Li, D. (2009). Strain transfer coefficient analyses for embedded fiber Bragg grating sensors in different host materials. *Journal of Engineering Mechanics*, *135*(12), 1343–1353. https://doi.org/10.1061/(ASCE)0733-9399(2009)135:12(1343)

Lienhart, W. (2015). Case studies of high-sensitivity monitoring of natural and engineered slopes. *Journal of Rock Mechanics and Geotechnical Engineering*, *7*(4), 379–384. https://doi.org/10.1016/j.jrmge.2015.04.002

Lindsey, N. J., Martin, E. R., Dreger, D. S., Freifeld, B., Cole, S., James, S. R., et al. (2017). Fiber-optic network observations of earthquake wavefields. *Geophysical Research Letters*, *44*, 11,792–11,799. https://doi.org/10.1002/2017GL075722

Linker, R., & Klar, A. (2017). Detection of sinkhole formation by strain profile measurements using BOTDR: Simulation study. *Journal of Engineering Mechanics*, *143*(3), B4015002. https://doi.org/10.1061/(ASCE)EM.1943-7889.0000963

Massonnet, D., & Feigl, K. L. (1998). Radar interferometry and its application to changes in the Earth's surface. *Reviews of Geophysics*, *36*(4), 441–500. https://doi.org/10.1029/97RG03139

Moore, J. R., Gischig, V., Button, E., & Loew, S. (2010). Rockslide deformation monitoring with fiber optic strain sensors. *Natural Hazards and Earth System Science*, *10*(2), 191–201. https://doi.org/10.5194/nhess-10-191-2010

Murai, D., Kunisue, S., Higuchi, T., & Kokubo, T. (2013). In-situ formation compaction monitoring in deep reservoirs by use of fiber optics. In *EGU general assembly 2013* (pp. EGU2013–EGU3860). Vienna, Austria: European Geosciences Union.

Peltier, A., Staudacher, T., Catherine, P., Ricard, L.-P., Kowalski, P., & Bachèlery, P. (2006). Subtle precursors of volcanic eruptions at Piton de la Fournaise detected by extensometers. *Geophysical Research Letters*, *33*, L06315. https://doi.org/10.1029/2005GL025495

Picarelli, L., Damiano, E., Greco, R., Minardo, A., Olivares, L., & Zeni, L. (2015). Performance of slope behavior indicators in unsaturated pyroclastic soils. *Journal of Mountain Science*, *12*(6), 1434–1447. https://doi.org/10.1007/s11629-014-3104-3

Plinninger, R. J., Alber, M., & Düllmann, J. (2010). The influence of casing and backfilling materials on inclinometer measurements. In A. L. Williams, G. M. Pinches, C. Y. Chin, T. J. McMorran, & C. I. Massey (Eds.), *Geologically active* (pp. 2361–2367). Auckland, New Zealand: CRC Press.

Puzrin, A. M., Iten, M., & Fischli, F. (2020). Monitoring of ground displacements using borehole-embedded distributed fibre optic sensors. *Quarterly Journal of Engineering Geology and Hydrogeology*, *53*(1), 31–38. https://doi.org/10.1144/qjegh2018-166

Rabaiotti, C., Iten, M., & Fischli, F. (2015). Implementation of fibre-optic vertical extensometers for safety monitoring. In P. Dight (Ed.), *Proceedings of the Ninth Symposium on Field Measurements in Geomechanics* (pp. 631–644). Perth, WA, Australia: Australian Centre for Geomechanics.

Sasaki, T., Park, J., Soga, K., Momoki, T., Kawaguchi, K., Muramatsu, H., et al. (2019). Distributed fibre optic strain sensing of an axially deformed well model in the laboratory. *Journal of Natural Gas Science and Engineering*, *72*, 103028. https://doi.org/10.1016/j.jngse.2019.103028

Satyabala, S. P. (2006). Coseismic ground deformation due to an intraplate earthquake using synthetic aperture radar interferometry: The M_w6.1 Killari, India, earthquake of 29 September 1993. *Journal of Geophysical Research*, *111*, B02302. https://doi.org/10.1029/2004JB003434

Schenato, L. (2017). A review of distributed fibre optic sensors for geo-hydrological applications. *Applied Sciences*, *7*(9), 896. https://doi.org/10.3390/app7090896

Schenato, L., Palmieri, L., Camporese, M., Bersan, S., Cola, S., Pasuto, A., et al. (2017). Distributed optical fibre sensing for early detection of shallow landslides triggering. *Scientific Reports*, *7*(1), 14,686. https://doi.org/10.1038/s41598-017-12610-1

Shi, B., Zhang, D., & Zhu, H.-H. (2019). *Distributed fiber optic sensing for geoengineering monitoring* (1st ed.). Beijing, China: Science Press. (in Chinese)

Sleeman, R., Haak, H. W., Bos, M. S., & van Gend, J. J. A. (2000). Tidal tilt observations in the Netherlands using shallow borehole tiltmeters. *Physics and Chemistry of the Earth, Part A: Solid Earth and Geodesy*, *25*(4), 415–420. https://doi.org/10.1016/S1464-1895(00)00065-X

Soga, K., & Luo, L. (2018). Distributed fiber optics sensors for civil engineering infrastructure sensing. *Journal of Structural Integrity and Maintenance*, *3*(1), 1–21. https://doi.org/10.1080/24705314.2018.1426138

Thévenaz, L. (2010). Brillouin distributed time-domain sensing in optical fibers: State of the art and perspectives. *Frontiers of Optoelectronics in China*, *3*(1), 13–21. https://doi.org/10.1007/s12200-009-0086-9

Wang, B., Li, K., Shi, B., & Wei, G. (2009). Test on application of distributed fiber optic sensing technique into soil slope monitoring. *Landslides*, *6*(1), 61–68. https://doi.org/10.1007/s10346-008-0139-y

Xiang, P., & Wang, H. (2018). Optical fibre-based sensors for distributed strain monitoring of asphalt pavements. *International Journal of Pavement Engineering*, *19*(9), 842–850. https://doi.org/10.1080/10298436.2016.1211872

Zhang, C.-C., Shi, B., Gu, K., Liu, S.-P., Wu, J.-H., Zhang, S., et al. (2018). Vertically distributed sensing of deformation using fiber optic sensing. *Geophysical Research Letters*, *45*(21), 11,732–11,741. https://doi.org/10.1029/2018GL080428

Zhang, C.-C., Zhu, H.-H., & Shi, B. (2016). Role of the interface between distributed fibre optic strain sensor and soil in ground deformation measurement. *Scientific Reports*, *6*(1), 36,469. https://doi.org/10.1038/srep36469

Zhang, Y., & Xue, Z. (2019). Deformation-based monitoring of water migration in rocks using distributed fiber optic strain sensing: A laboratory study. *Water Resources Research*, *55*, 8368–8383. https://doi.org/10.1029/2019WR024795